



SEMINÁRIOS PPG-EM / UERJ 2019

PPG-EM UERJ 2019 SEMINARS

**Programa de Pós-graduação em Engenharia
Mecânica UERJ**

Graduate Program in Mechanical Engineering UERJ



SEMINÁRIOS PPG-EM / UERJ 2019

PPG-EM UERJ 2019 SEMINARS

**Programa de Pós-graduação em Engenharia
Mecânica UERJ**

Graduate Program in Mechanical Engineering UERJ



WWW.PPGEM.UERJ.BR

Editado por Prof. Daniel J. N. M. Chalhub.

Reprodução é permitida sem restrições. O layout foi criado a partir do modelo \LaTeX “The Legrand Orange Book”, versão 2.1 (14/11/2015), sob a licença Creative Commons:

CC BY-NC-SA 3.0 (<http://creativecommons.org/licenses/by-nc-sa/3.0/>)

Capa: “*SIM! A Terra é redonda*”. Créditos de imagem: Usuário Wilkimages do Pixabay
<https://pixabay.com/photos/earth-globe-planet-world-space-11015/>

Foto dos cabeçalhos: “*A Terra de noite*”. Créditos de imagem: Usuário Free-Photos do Pixabay
<https://pixabay.com/photos/earth-lights-environment-globe-1149733/>

Edited by Prof. Daniel J. N. M. Chalhub.


There are no restrictions for reproducing this material. The layout was created from the \LaTeX template “The Legrand Orange Book”, version 2.1 (14/11/15), under the Creative Commons license:

CC BY-NC-SA 3.0 (<http://creativecommons.org/licenses/by-nc-sa/3.0/>)

Cover: “*YES! The Earth is round*”. Image by Pixabay user Wilkimages
<https://pixabay.com/photos/earth-globe-planet-world-space-11015/>

Header image: “*The Earth at night*”. Image by Pixabay user Free-Photos
<https://pixabay.com/photos/earth-lights-environment-globe-1149733/>

March 15, 2021



Sumário / Contents

1	Mini-artigos / Short papers	11
	1st Seminar – April 04, 2019	
1.1	Erika Castanho Magalhães de Moraes	12
	<i>COMPUTATIONAL SIMULATION OF ENERGY PERFORMANCE OF HVAC ALTERNATIVE SOLUTIONS FOR A BANK BRANCH</i>	
	2nd Seminar – May 21, 2019	
1.2	João Paulo Alves Barros	14
	<i>NUMERICAL SOLUTIONS TO THE DISPERSION POLLUTION PROBLEM IN RODRIGO DE FREITAS LAGOON</i>	
	3rd Seminar – June 18, 2019	
1.3	Bianca Marques	16
	<i>PERFORMANCE EVALUATION OF A METALLIC COATING BY THERMAL ARC SPRAY PROCESS IN CONDITIONS WITH AND WITHOUT SEALANT</i>	
1.4	Diego Moreira da Silva	18
	<i>NANOCOMPOSITES FOR 3D PRINTING</i>	
1.5	Gesué dos Santos Valle Rezende	20
	<i>TECHNICAL AND ECONOMIC VIABILITY ANALYSIS OF AN ORGANIC RANKINE CYCLE WITH COMPOUND PARABOLIC CONCENTRATOR SOLAR COLLECTOR</i>	

1.6 Thamires Lima da Paixão Bernardes 22
EVALUATION ON USING WEATHER DATA FROM CITIES LISTED IN THE NBR 16401 FOR AIR CONDITIONING DESIGN IN NON-LISTED CITIES

1.7 Marcelo André Cordeiro da Silva 24
POOL FIRE AND THERMAL RADIATION MODELING USING COMPUTATIONAL FLUID DYNAMICS

4th Seminar – June 25, 2019

1.8 Diego de Lima Gomes 26
ANALYSIS OF MECHANICAL CHARACTERISTICS OF A POLYMER-MATRIX COMPOSITE REINFORCED WITH RESIDUES FROM BRAZILIAN COAL-FIRED THERMAL POWER PLANT

5th Seminar – July 12, 2019

1.9 Juan Carlos Azeredo Coutinho 28
ELECTRIC VEHICLE WITH PHOTOVOLTAIC POWER SOURCE

1.10 Leonardo Paiva Ferreira da Costa 30
APPLICATION OF THE CHARACTERISTIC FUNCTION METHOD TO OBTAIN THE NON-LINEAR INTEGRAL TRANSFORM FOR AT-INSAR PHASE SPECTRUM

6th Seminar – October 29, 2019

1.11 Álvaro Eduardo do Amaral Menezes Júnior 32
ASSESSMENT OF THE DYNAMIC RESPONSE AND FATIGUE ANALYSIS OF FLOORS SUBJECTED TO ACTION OF MECHANICAL EQUIPMENT

7th Seminar – December 03, 2019

1.12 André Patrocínio de Castro 34
ANALYSIS OF AIR CIRCULATION AND HYGROTHERMAL BEHAVIOR OF THE UNIVERSE MUSEUM (GÁVEA PLANETARIUM)

1.13 Luís Henrique Carnevale da Cunha 36
SEMI-LAGRANGEAN METHOD APPLIED IN THE CONJUGATED HEAT PROBLEM USING AN AXISYMMETRICAL STREAM FUNCTION-VORTICITY FORMULATION

1.14 Victor Vieira Maudonet 38
UNCERTAINTIES QUANTIFICATION ON CREEP REMAINING LIFE PREDICTION MODELS

1.15 Alexandre Vasconcelos Rodrigues 40
EVALUATION OF THERMAL AND EVAPORATIVE EFFICIENCY OF SPRAY-DRYER

1.16 Diego Matos Silva Lopes **42**
A DATA-DRIVEN APPROACH FOR INFERENCE OF THE EVOLUTION EQUATION OF A DUFFING OSCILLATOR

1.17 Marcos Vinicius Issa **44**
EMPLOYING 0-1 TEST FOR CHAOS TO CHARACTERIZE THE CHAOTIC DYNAMICS OF A GENERALIZED GAUSS ITERATED MAP

8th Seminar – December 10, 2019

1.18 Alane Miguelis Falcão Magalhães **46**
THE PIECEWISE CONSTANT THERMAL CONDUCTIVITY AND THE KIRCHHOFF TRANSFORMATION

1.19 Daniel Lessa Coelho **48**
ORIENTATION EFFECTS IN DISSIPATIVE STRUCTURES: NUMERICAL STUDY OF THE NONUNIFORMLY FORCED SWIFT-HOHENBERG EQUATION

1.20 Gabriel Guimarães Oliveira **50**
UASB (UPFLOW ANAEROBIC SLUDGE BLANKET) REACTORS SIMULATOR BASED ON ADM1

1.21 José Ricardo da Silva Cerqueira Junior **52**
MATHEMATICAL MODELLING AND SIMULATION OF TRANSIENT STATE HEAT TRANSFER PROCESS IN A RIGID BODY WITH TEMPERATURE-DEPENDENT THERMAL CONDUCTIVITY

9th Seminar – December 17, 2019

1.22 Frederico Garcia B. Lacerda **54**
QUANTIFICATION OF DEFECTS IN THERMAL SPRAY COATINGS USING DIGITAL IMAGE PROCESSING

1.23 José Elias de Oliveira Gomes Júnior **56**
OPTIMUM DESIGN OF AN URBAN BUS CHASSIS BASED ON GENETIC ALGORITHMS AND FINITE ELEMENT METHOD SIMULATIONS

1.24 Matheus Costa Ximenes **58**
USE OF FOCUSED ION BEAM OF GALLIUM AND HELIUM FOR LITHOGRAPHIC DRAWINGS OF METROLOGICAL PATTERNS IN A SILICON SAMPLE



1. Mini-artigos / Short papers

15 de março de 2021

Neste capítulo são apresentados os mini-artigos dos vinte e quatro trabalhos científicos que fizeram parte dos Seminários do PPG-EM em 2019. Os trabalhos estão organizados segundo a data de apresentação.

Prof. Daniel J. N. M. Chalhub, D.Sc.
Coordenador dos Seminários PPG-EM 2019

March 15, 2021

This chapter presents the short papers of the twenty-four scientific works that participated in the PPG-EM Seminars in 2019. Papers are organized according to the date of presentation.

Prof. Daniel J. N. M. Chalhub, D.Sc.
PPG-EM 2019 Seminars Chair



COMPUTATIONAL SIMULATION OF ENERGY PERFORMANCE OF HVAC ALTERNATIVE SOLUTIONS FOR A BANK BRANCH

Author: Erika Castanho Magalhães de Morais¹ moraisecm@gmail.com
Advisor(s): Manoel Antônio da Fonseca Costa Filho¹

¹ Rio de Janeiro State University

PPG-EM Seminars: season 2019
<http://www.ppgem.uerj.br>

April 16, 2019

Keywords: Energy Efficiency, Hourly Analysis Program, Bank Branch, HVAC.

1 Introduction

The energy consumption of commercial and residential buildings corresponds to 50.8 % of the energy consumption in Brazil [4], and air conditioning systems can correspond to more than 50 % in relation to the total consumed in these buildings, for this reason, energy efficiency projects usually start replacing inefficient equipment and changing the habits of its users. The importance of this follow-up of the Heating, Ventilation and Air Conditioning (HVAC) in the energy scenario is growing either by the new constructive tendency of residential and commercial buildings, or by climate change or the expansion of urban centers. The efficiency improvement of equipment and systems as well as other actions to reduce the emission of carbon dioxide to atmosphere should be considered by the engineers, either with the improvement in the design of heat exchangers, development of new more sustainable refrigerant fluids, investment in automation and control and in development of designs aligned with the energy efficiency targets. The design of an efficient air conditioning system is influenced by several parameters such as the construction materials used, local climatic conditions, solar orientation, type of occupation, type of air conditioning system and its performance coefficient, air quality requirement, hours of operation and internal conditions to be achieved. The reduction of consumption and the financial return of investment in energy efficiency actions for HVAC systems vary with the type of application. In the case of bank branches, where there is a high occupancy rate, the cost of HVAC represents a significant part of the operational cost of the building and the application of energy efficiency strategies present significant results in the short term. Studies that address energy analysis in air conditioning systems applied to bank branches are infrequent in the literature as well as analysis using the software Hourly Analysis Program (HAP). Some works of computer simulation using the software HAP are found in the literature, among which we can highlight the work developed by [6] that carried out simulation of several

scenarios applied to the system of climatization of chemical laboratories with the use of energy recovery, chilled beams and systems with variable air flow (VAV). In this type of application, the airflows of renovation are extremely high, and may even demand 100% of outdoor air. We also cite the work of [1], who performed the simulation of a chilled water air conditioning system with constant and variable air flow air treatment units, using the Energy Plus and HAP programs for a coffee shop.

2 METHODOLOGY

The study case is a commercial building dedicated to banking activities located in the north zone of the city of Rio de Janeiro. Currently, the ground floor, mezzanine and 1st floor is air conditioned by indirect expansion system and the last floor by direct expansion systems. The subsoil is not conditioned and has no occupation. The indirect expansion system consists of two screw type air cooled chillers with a capacity of 55.39 TRs each, two 15 CV cold water pumps, one of which is a reserve, and 11 air treatment units (ATU), formed by 4 units of 5 TRs, 4 units of 7.5 TRs and 3 units of 10 TRs. The direct expansion system consists of high capacity splits, which add up to 50 TRs, being a 5 TRs equipment and 3 of 15 TRs. The occupancy data used for the restricted environments were obtained by local survey and for the public service areas the occupancy density foreseen in the standard was used.[3] The operating schedule for the air conditioning and lighting systems was established Monday through Friday, from 8:00 AM to 6:00 PM. The values of heat dissipation of the lamps, reactors and equipment were obtained from the standard.[3] The heat transfer coefficients of the envelope were calculated according to standard.[2] The indoor temperature was established for comfort purposes, with a dry bulb temperature of 24 °C for summer conditions and 22 °C for winter conditions.[5] The renewal air flow rate was determined by finding the higher value between the recommended by [5] and level 1 [3]. The simulations were performed using the HAP, considering the six scenarios described below, maintaining the weather conditions, conditioned space characteristics, thermostat parameters, lighting, occupation and equipment schedules, air

renewal rates and characteristics of building envelope. Simulation 1: The current air conditioning system was performed. The efficiency ratings of the chiller and the high capacity splits are, respectively, 2.9 kW / kW and 2.86 kW / kW. Simulation 2: This simulation was performed considering the installation of air-cooled chillers. Air renewal is performed through a G4 filter unit .[3] The energy efficiency rate (EER) considered was 3.10 kW / kW. Simulation 3: This simulation was based on the last, altering the air dispensing form through installation of VAV boxes and use of inverter in the ventilator of the ATU. It was also considered the use of primary circulation of cold water with variable flow. The EER considered was 3.10 kW / kW. Simulation 4: This simulation was performed considering the same configuration of simulation 3 with the addition of an energy recovery ventilator. Simulation 5: This simulation was performed considering the use of high capacity split equipment. The EER considered was 3,224 kW / kW. Air renewal is performed through the G4 filter unit.[3] Simulation 6: This simulation was performed considering a Variable Refrigerant Flow (VRF) system. It was also considered a sensitive heat recovery plate system for external air preconditioning.

3 Results

The simulations were completed presenting satisfactory results and allowing the comparison of different configurations of the air conditioning systems. Simulation 1 was performed for energy diagnosis of the existing system where it was verified that the system is oversized. All simulated scenarios were more advantageous from the point of view of energy consumption compared to this system with reductions between 5,63 % and 46.69 %. Figure (1) shows the annual energy cost for HVAC system operation. The simulation 6 was the most favorable from the point of view of the energy performance, presenting consumption 43.51 % smaller when compared to simulation 2. The cost associated with the fans was also significant in all simulated systems ranging from 15.68 % to 32,45 % of the total cost associated with the HVAC system. In this sense, the adoption of air handling units with variable air flow showed a reduction of 49.11 % in the annual consumption referring to this item. Figure (2) shows the behavior of energy demand by the HVAC system throughout the year. The total energy consumption of systems 3 and 5 were very close throughout the year, being more favorable for system 3 in the months of May to November. Simulation 6 showed higher energy efficiency throughout the year.

4 Conclusions

The use of a direct expansion system in this study case is advantageous considering from the scenarios with simpler systems, as in simulations 2 and 5. Among the scenarios that consider systems of greater complexity and with sophisticated control and automation requirements, as in simulations 3 and 6, the VRF system presented better energy performance. Considering that the HVAC system represents between 47.66 % e 32.68 %

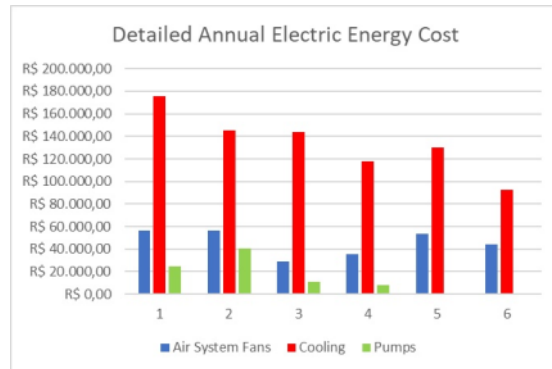


Figure 1: Detailed Annual Electric Energy Cost

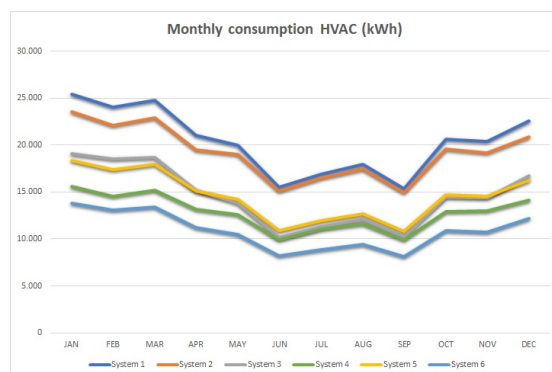


Figure 2: Monthly Consumption HVAC

of the total cost of the building, it is possible to obtain an economy from 2.68 % to 13.61 % in relation to the total consumption of the building with the adoption of the systems 2 and 5 and a saving of 13.61 % a 22.25 % in relation to the total consumption of the building with the adoption of Variable Air Volume or Variable Refrigerant Flow systems.

References

- [1] Inês Alves de Frias Pinto. Projeto de avac e simulação energética de uma cafeteria. Master's thesis, ISEL, 2013.
- [2] Associação Brasileira de Normas Técnicas ABNT. Desempenho térmico de edificações. Technical report, 2005.
- [3] Associação Brasileira de Normas Técnicas ABNT. Nbr-16401 instalações de ar condicionado – sistemas centrais e unitários. Technical report, 2008.
- [4] Empresa Brasileira de Pesquisa Energética EPE. Relatório final balanço energético nacional 2018 – ano base 2017. Technical report, 2018.
- [5] Agência Nacional de Vigilância Sanitária – ANVISA. Resolução 9: Padrões referenciais de qualidade do ar interior em ambientes climatizados artificialmente de uso público e coletivo. Technical report, 2003.
- [6] Felipe Alfaia do Carmo. Simulação computacional do desempenho energético da edificação laboratorial, radial 8, do cenpes/petrobras. Master's thesis, PPGEM/UERJ, 2017.



NUMERICAL SOLUTIONS TO THE DISPERSION POLLUTION PROBLEM IN RODRIGO DE FREITAS LAGOON.

Author: João Paulo Alves Barros¹ jpab_7@hotmail.com
Advisors: Cristiane Oliveira de Faria¹; João Frederico Da Costa Azevedo Meyer²
¹ Rio de Janeiro State University
² IMECC/UNICAMP

PPG-EM Seminars: season 2019
<http://www.ppgem.uerj.br>

May 21, 2019

Keywords: Finite element method, Crank-Nicolson method, Dispersion pollution, Rodrigo de Freitas lagoon.

1 Introduction

Environmental pollution is one of the biggest problems of this century. The main factors that has influenced this type of problem is the rapid industrial growth on a global scale combined with the emission of pollutants. Pollution occurs in several ways, such as: greenhouse effect, changes in mortality rates and birth rates of some species, destruction of the ozone layer, acid rain, among others. The factors cited hinder not only the life of the planet but also human longevity.

The aim of this work is to study and monitor the level of pollution dispersion of the Rodrigo de Freitas lagoon by effluents. This focus is given by several motivations, one of them is to predict the contamination process over time using the Finite Element (FEM) method for space discretization combined the Crank-Nicolson method for temporal discretization. Numerical simulations are presented comproving results expecteds.

2 The model problem

The problem of treatment and dispersion of pollution will be modeled by the transport equation, a partial differential equation widely found in ecology problems. In this study we will consider two-dimensional case, that is, $\Omega \subset \mathbb{R}^2$.

Let $c(t, x, y)$ be the concentration of pollutant with $(x, y) \in \mathbb{R}^2$ at time $t \in I = (0, T]$ given by:

$$\begin{cases} \frac{\partial c}{\partial t} - \epsilon \Delta c + \beta \cdot \nabla c + \delta c = f & \text{in } \Omega, \\ -\epsilon \frac{\partial c}{\partial \eta} = 0 & \text{on } \Gamma. \end{cases} \quad (1)$$

Each term in the equation has a meaning that is described below:

- **Diffusion Transport:** The term $\epsilon \Delta c$ defines the diffusion term where ϵ is the diffusibility constant of the pollutant, which will be considered constant.
- **Convection Transport:** The term $\beta \cdot \nabla c$ is defined as the convective term and β is the velocity

field, as $\beta = u\hat{i} + w\hat{j}$ and $\nabla \cdot \beta = 0$.

- **Reaction Transport:** The term δc is defined as the decay term, that is, the loss of the pollutant in the system. The constant δ is defined as the decay rate in the aquatic environment.
- **Term Source:** The term source known in Ω is given by f . It can be one or more sources of pollutants.
- **Neumann Boundary Condition:** It was considered that the boundary lagoon is coated with concrete and does not lose pollutants by the edge.

3 Proposed methodology

In this study it was considered a numerical methodology using the Galerkin Method for space discretization combined with the Crank-Nicolson method for temporal discretization. Therefore, the model problem (1) is rewritten as,

$$\begin{aligned} & \sum_{j=1}^N c_j^{n+1} \left[\left(1 + \frac{\delta \Delta t}{2}\right) (\phi_j, \phi_i)_\Omega + \frac{\epsilon \Delta t}{2} (\nabla \phi_j, \nabla \phi_i)_\Omega \right. \\ & \quad \left. + \frac{u \Delta t}{2} \left(\frac{\partial \phi_j}{\partial x}, \phi_i\right)_\Omega + \frac{w \Delta t}{2} \left(\frac{\partial \phi_j}{\partial y}, \phi_i\right)_\Omega \right] \\ & = \sum_{j=1}^N c_j^n \left[\left(1 - \frac{\delta \Delta t}{2}\right) (\phi_j, \phi_i)_\Omega - \frac{\epsilon \Delta t}{2} (\nabla \phi_j, \nabla \phi_i)_\Omega \right. \\ & \quad \left. - \frac{u \Delta t}{2} \left(\frac{\partial \phi_j}{\partial x}, \phi_i\right)_\Omega - \frac{w \Delta t}{2} \left(\frac{\partial \phi_j}{\partial y}, \phi_i\right)_\Omega \right] + \Delta t (f, \phi_i)_\Omega, \end{aligned} \quad (2)$$

where $\Delta t = T/n$ and n is the number of time steps. The approximate solutions have been obtained using bilinear triangular elements, P_1 , with lagrangean interpolation functions.

4 Simulations

In order to perform the simulations, a map from Rodrigo de Freitas lagoon was extract using *Google Earth Pro* and a mesh was built-in by the software Gmsh, a 3D finite element mesh generator. In Figure 1 we see the mesh resulting considering triangle elements.

The lagoon was partitioned into 751 elements, the initial pollution, c_0 will be given as 0, and 1 node (node 33) will be chosen as the only source of pollution at the

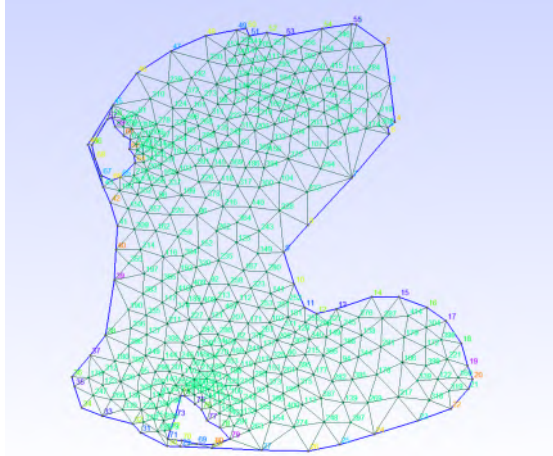


Figure 1: Discretization in triangular elements using GMSH.

lagoon.

The Table 1 shows the values used in this study. The parameters of diffusion, velocity field and decay were based on previous studies in [1] and [2].

Table 1: Values parameters at the simulation

Parameters	values
ϵ	$0.4 \text{ km}^2/\text{h}$
β	1.9 km
w	0.02 km/h
u	0.02 km/h
δ	10^{-10} h^{-1}
c_0	0
T	30 h
N_e	751
δt	0.03 h
node 33	0.14

4.1 Results

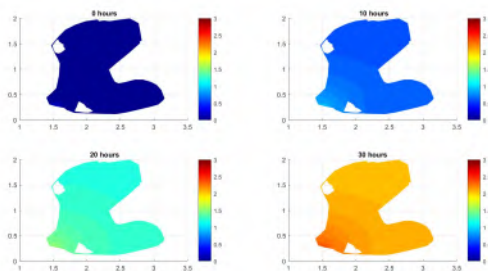


Figure 2: Analysis of the dispersion of pollution over time.

In Figures 2 and 3 we can see a concentration over four times. We can observe that the concentration of pollution increases over time in the lagoon, which was expected because the lagoon does not lose pollutants at the edge.

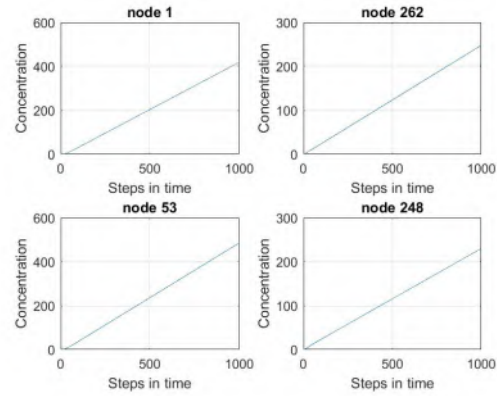


Figure 3: Analysis of the concentration of pollution along the time steps.

5 Conclusions and Futures perspectives

The program solved the dispersion problem satisfactorily. It can be analyzed that the analysis of the concentration over time occurs as expected, since the lagoon does not lose pollutants, so the total concentration increases. The next step will be to analyze the dispersion process in a larger scenario and in addition will be used sources of pollution and sinks.

The partition of the lagoon into triangular elements was done using the GMSH software. A future approach that can be given is also to work with not only surface pollution, such as the one inside the lagoon, but a 3D case. A simulation closer than the real case that was studied in [2].

6 Acknowledgments

I would like to express my acknowledgment for Capes, that supported the development of this research, PPGEM-UERJ and for Unicamp for all the given support during my visit to Campinas for the purpose of elaborating the project.

References

- [1] Leidy Diane et al. Modelagem e simulações do comportamento evolutivo de poluentes em corpos aquáticos de grande extensão: o caso da represa do rio manso. Master's thesis, UNICAMP.
- [2] G.L Diniz. *Dispersão de Poluentes num Sistema Ar-Água: Modelagem, Aproximação e Aplicações*. PhD thesis, UNICAMP.



PERFORMANCE EVALUATION OF A METALLIC COATING BY THERMAL ARC SPRAY PROCESS IN CONDITIONS WITH AND WITHOUT SEALANT

Author: Bianca Marques¹ bianca_bmarques@yahoo.com.br
Advisor(s): Marilia Diniz¹

¹ Rio de Janeiro State University

PPG-EM Seminars: season 2019
<http://www.ppgem.uerj.br>

June 18, 2019

Keywords: Boiler, corrosion, coating, sealant.

1 Introduction

The internal tubes of a boiler are examples of mechanical components that suffer wear by operating at high temperature and abrasive environment. Thus the reinforcement of the surface of these components, by applying a coating, it is quite interesting for protection against corrosion and mechanical wear [3]. Thermal Arc Spray Process is a low-cost and high-productivity technique, however it produces coatings with some porosity [1]. The presence of defects will affect the corrosion resistance of the coatings and the use of sealants that fall into these defects will increase the action of this base material protection system [2]. The objective of this work is to evaluate the use of metallic coating obtained by Thermal Arc Spray Process in the conditions with and without sealant in the protection of steel pipes for corrosion and wear caused by the aggressive environment of boilers operating with untreated water and with the presence of aggressive ions to their pipes.

2 Methodology

A sample immersion device was designed for a medium pressure gas boiler of a pharmaceutical industry in Rio de Janeiro state. Semi-quantitative chemical analysis by Energy Dispersive Spectroscopy (EDS) of sprayed layer and of sealant applied and sealant layer thickness measurements on images obtained by Scanning Electron Microscopy (SEM) using the Image J software (FIJI) was performed in the samples before immersion in the boiler environment. six samples, three with sealant and three without, were used. in periods of 3 months, totaling 9 months from the insertion of the samples inside the boiler, a sample with sealant and other without will be withdrawn and passed through the same analyses done before insertion.

3 Results

The chemical composition of the consumable used for spraying and the coating chemical composition detected by EDS are shown in Table 1.

Table 1: Quantitative chemical composition of consumable used in the Thermal Arc Spray Process and semi quantitative coating chemical composition found by EDS technique.

	consumable used	arc spray coating
Cr	13.20	14.53
Nb	6.00	8.72
Ni	5.50	5.28
B	4.20	
Al	2.00	1.88
Mn	1.30	0.72
Si	1.20	1.67
Fe	balance	balance

Figure (1) exemplifies the spectrum obtained by EDS of the sprayed layer area.

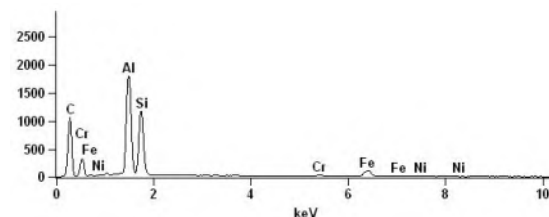


Figure 1: Energy spectrum characteristic of coating region analyzed in Fig. (2).

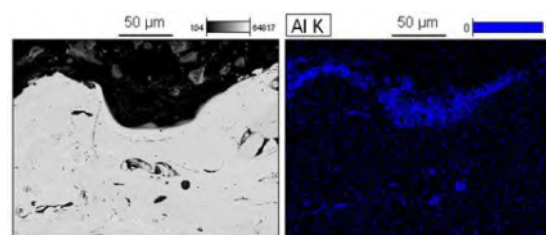


Figure 2: Sealant area analysed by EDS technique.

The sealant layer thickness fund was around 20 μm according to measures made in FIJI as shown in Fig. (3).

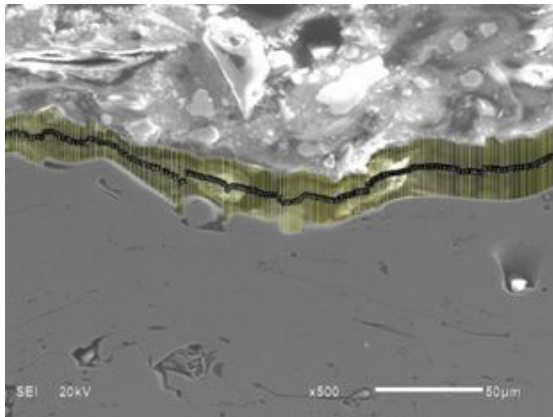


Figure 3: Sealant thickness measurement using the FIJI software.

4 Discussion and conclusion

- The chemical composition of the consumable used for spraying and the coating chemical composition detected by EDS are fully compatible;
- Boron is not identified by EDS because of your low atomic weight;
- Was verified the high aluminum and silicon indices into the sealant;
- The sealant layer thickness fund was 40% less than specified by the manufacturer (almost 50 μm);
- In the end of the study is expected results that lead us to affirm the indication or not of the material tested for the environment and operating conditions of the gas boiler.

References

- [1] BERNDT C.C. et.al. *Handbook of Thermal Spray Tecnology*. ASM International, 2004.
- [2] SULZER. Technical information, an introduction to thermal spray. Technical report, Sulzer, 2013.
- [3] BRITO V.R. Caracterização de revestimentos metálicos aspergidos termicamente por arco elétrico. Master's thesis, CEFET-RJ, April 2010.



NANOCOMPOSITES FOR 3D PRINTING

Author: Diego Moreira da Silva¹ diego-mattias@hotmail.com
Advisors: José Brant de Campos¹ ; Eric Cardona Romani²

¹ Rio de Janeiro State University

² Instituto SENAI de Tecnologia Automação e Simulação

PPG-EM Seminars: season 2019
<http://www.ppgem.uerj.br>

jun 18, 2019

Keywords: Nanocomposite; PLA graphene; 3D printing;

1 Introduction

In recent years, graphene has attracted great attention from physics and research communities because of its atomic thickness, excellent mechanical, thermal, optical and electrical properties. 3D printing is a process for creating 3D physical objects from a 3D digital model. The use of graphene composites integrated with a 3D printing can generate materials with distinct reinforcement and wear properties compared to a graphene-free polymer matrix[7][3]. Graphene combined with polylactic acid creates a conductive nanocomposite with distinct mechanical properties[2]. In many cases, the 3D graphene nanocomposite acts as a protective film and can avoid future wear problems and prolong the life of the composite. In this work we report the methodology to realize the nanocomposite polymer-graphene, to endorse its applications in wear and protection. In this work, the FDM tool[1] was used to produce graphene-polylactic acid nanocomposites and the samples were studied by Scanning Electron Microscopy (SEM), Raman Spectroscopy and hardness and tribology measurements.

2 Methodology

For the production of samples via 3D printer were purchased filaments of PLA and PLA graphene from the company Black Magic. Through the FDM technique samples were printed in a 15-millimeter cube format, based on STL drawings read by the Repetier Host. Among the printing parameters some were fixed while others were varied aiming a surface with low levels of irregularities. Cetr UMT Multi-Specimen Test system A linear reciprocal test with a normal force of 0.3 Newtons and a velocity of 10 mm / s and a displacement amplitude of 10 mm, where the counterpart is balls of AISI 302 steel of 6.0 mm diameter and Vickers hardness: 413. The macrometric images were obtained by the stereoscope of the ZEISS brand, while the nanometric images were obtained by the scanning electron microscope of the brand JOEL model JSM-7100F and Finally, Vickers (HV) microhardness tests were performed on the PAN-TEC model MV-1000A micro-meter with 50 gram load

and indentation time 15 seconds. The Raman technique was used to characterize the material.

3 Results and Discussion

The samples obtained by 3D printing from the commercial filament were characterized by the Raman spectrophotometry technique in order to evaluate if the product sent by the company really is the said material. It can be seen from figure 1 below:

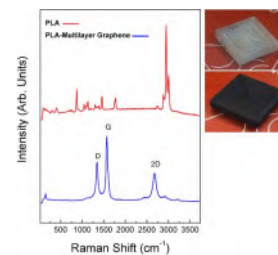


Figure 1: Raman of PLA and PLA graphene

With the confirmed material the cubic format samples were printed and their surfaces prepared for the wear test to obtain the coefficient of friction, the presence of graphene in the formation of composites reduces the coefficient of friction when compared to the matrix material, in this if the PLA. Figure 2 below shows the variation of the coefficient of friction with respect to time during the wear test.

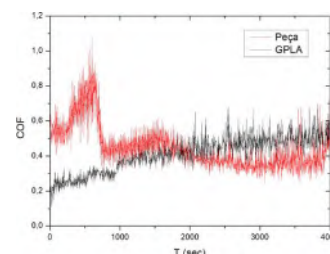


Figure 2: Variation of the coefficient of friction with respect to the time of PLA and PLA graphene

Up to 1800 seconds the sample containing graphene was shown to have higher wear resistance but for some reason the material became less resistant over time. The microhardness test was performed randomly on the

surface of the printed sample ensuring a safe distance from existing voids and cracks and generating hardness values of PLA and PLA graphene according to table 1 below:

Table 1: Hardness of PLA and PLA graphene

PLA	PLA graphene
17,092 HV	11,723 HV

With the use of the SEM, the topography was analyzed and with magnification the presence of nanotubes was observed, which can be seen in figure 3.

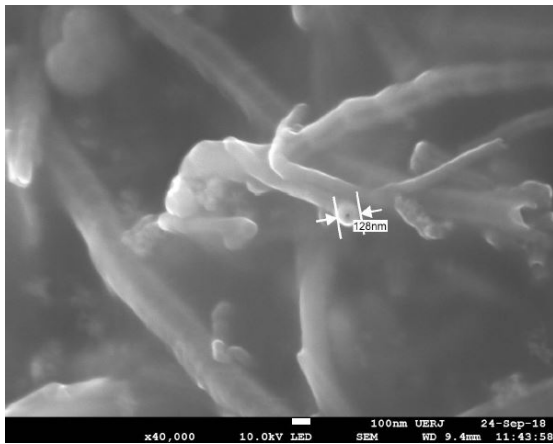


Figure 3: Carbon nanotubes in the sample of PLA graphene

The presence of carbon nanotubes in the composite should improve the mechanical properties compared to the pure matrix [4][6], but the wear resistance reduced with time during the wear test and the hardness presented smaller values in the vicker scale for the sample containing graphene. PLA tends to lose mechanical properties when it works alongside a material in the dispersed phase which has the capacity to absorb water by weakening the matrix [5].

4 Conclusion

The presence of graphene in the PLA has not improved its mechanical characteristics so far because graphene apparently has a good capacity to absorb moisture, which weakens the PLA matrix.

References

- [1] Sorin Cristian Albu. Development on the production of a new type of extruder used in additive manufacturing, fdm technology. *Procedia Manufacturing*, 22:141–146, 2018.
- [2] Patrick F Flowers, Christopher Reyes, Shengrong Ye, Myung Jun Kim, and Benjamin J Wiley. 3d printing electronic components and circuits with conductive thermoplastic filament. *Additive Manufacturing*, 18:156–163, 2017.
- [3] R Kotsilkova, E Ivanov, P Todorov, I Petrova, N Volynets, A Paddubskaya, P Kuzhir, V Uglov, I Biró, K Kertész, et al. Mechanical and electromagnetic properties of 3d printed hot pressed nanocarbon/poly (lactic) acid thin films. *Journal of Applied Physics*, 121(6):064105, 2017.
- [4] Bruno F. Machado and Philippe Serp. Catalysis science technology. *MINIREVIEW*, 2:54–75, 2012.
- [5] Philippe Dubois Marius Murariu. Pla composites: From production to properties. *Advanced Drug Delivery Reviews*, 107:17–46, 2016.
- [6] Luisa Pastrana-Martínez, Sergio Morales-Torres, Helder Gomes, and Adrián Silva. Nanotubos e grafeno: os primos mais jovens na família do carbono! *Química*, 128:21–27, 2013.
- [7] Yanwu Zhu, Shanthi Murali, Weiwei Cai, Xuesong Li, Ji Won Suk, Jeffrey R Potts, and Rodney S Ruoff. Graphene and graphene oxide: synthesis, properties, and applications. *Advanced materials*, 22(35):3906–3924, 2010.



TECHNICAL AND ECONOMIC VIABILITY ANALYSIS OF AN ORGANIC RANKINE CYCLE WITH COMPOUND PARABOLIC CONCENTRATOR SOLAR COLLECTOR

Author: Gesué dos Santos Valle Rezende¹ grezende2@hotmail.com
Advisor(s): Daniel J. N. M. Chalhub and Manoel A. da F Costa Filho¹
¹ Rio de Janeiro State University

PPG-EM Seminars: season 2019
<http://www.ppgem.uerj.br>

June 18, 2019

Keywords: Solar Energy, Rankine Cycle, Renewable Energy, Power Generation

1 Introduction

An Organic Rankine Cycle (CRO), operates at cooler temperatures, although it contains the same equipment as a traditional Rankine Cycle. As the working fluid, hydrocarbons in general with a high molecular mass, vaporize at lower temperatures, demand lower consumption of thermal power for mechanical power generation. Solar Compound Parabolic Concentrator (CPC) as a source of thermal energy. This replaces the combustion of fossil fuels in the boiler, becoming a source of renewable energy, avoiding the emission of greenhouse gases. In addition, it allows reaching temperatures higher than the solar collector's planes through a thermal fluid that can be water, oil or air

2 BACKGROUND

2.1 COMPOUND PARABOLIC CONCENTRATOR SOLAR COLLECTOR (CPC)

A concentrator solar collector uses optical systems, lenses or mirrors, capable of increasing the intensity of the radiation and with that can reach quite high temperatures. In order to reach the temperature range from 100°C to 300°C, the most efficient solar collector with the least price that is able to reach it should be chosen. CPC is the most appropriate in this case, the application of CPC lies in industrial process and power generation

The most used geometric form is the parabolic one whose focus is located in the absorber. This absorber is generally a metal tube with the treated surface, usually wrapped by a glass tube in order to minimize thermal losses. Inside the tube circulates a transfer fluid whose correct choice is fundamental to the efficiency of the equipment.

2.2 ORGANIC RANKINE CYCLE

The organic Rankine cycle (ORC) is identical to the Conventional Rankine Cycle, differing only in the working fluid, which is organic and can be hydrocarbons or

halogenated hydrocarbons among others, and enables mechanical energy to be obtained at low temperatures (100 to 300°C). The organic fluid, characterized by a molecular mass higher than that of water, which leads to a slower rotation of the turbine, lower pressures and no erosion of the metal parts and blades.

2.3 THE CPC-ORC COUPLED SYSTEM

The proposed solar heating system (SHS) coupled with the power generation system is presented in (figure 1). The HTF is circulating in closed circuit.

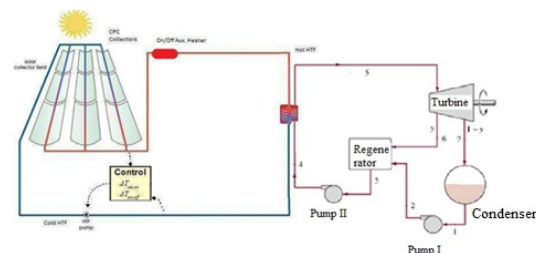


Figure 1

2.4 Equations

The concentration capacity represents the ability to intensify the radiation received by the absorber surface and is defined by the ratio between the collection area A_c (area receiving the radiation) and the absorption area A_{ab} .

$$C_b = \frac{A_c}{A_{ab}} \quad (1)$$

This definition, however, is only theoretical and presupposes an optically perfect system. Since several factors influence the concentration, one can define a point concentration factor, C_x , as the ratio between the incident radiation intensity at a given point in the absorptive plane and the direct solar radiation intensity reaching the opening plane of the collector

$$C_x = \frac{I_r(x)}{I_b} \quad (2)$$

2.5 Citations

Similar and even studies have already been carried out. The case of [1] for example, analyzed an organic rankine cycle driven by the exhaust gases of a combustion engine.

[4] performed a performance analysis of the cycle with several fluids until arriving at the one that brought the best yield to the cycle

A CRO triggered by a CPC was the subject of [2]. For this, meteorological data were collected from the region where the collector would be installed. We sought to balance the collector efficiency with cycle efficiency.

Also used was the thermodynamic study applied to the parabolic collector compound solar concentrator [3], which uses a non-flammable fluid, which does not change the viscosity, to transport the solar energy, converted into thermal energy.

3 Conclusions

The results will be presented in the development of this article, the results modeled in the Trnsys for (CPC) and Engineering Equation Solver (EES) for (ORC). Based on the pre-selected parameters, such as meteorological data, thermodynamic properties of the fluids and possible premised data, allowing the possible conclusions about technical-economic feasibility, opportunities for improvement, possible deficiencies and other conclusions that may increase the work

4 Acknowledgments

The authors thank to Prof. Gustavo R. dos Anjos for sharing insights and ideas in developing the PPG-EM's academic templates.

References

- [1] Valmir DE OLIVEIRA JUNIOR. A propose for an organic rankine cycle cogeneration system, 2019.
- [2] Antonio GARRIDO GALLEGO. Thermodynamic analysis of the power generation system of organic rankine with the solar heating system. In *17th Brazilian Congress of Thermal Sciences and Engineering*, Águas de Lindóia, SP, 2018.
- [3] Ahmed Elsayed Ismail. Usind compound parabolic concentration solar collector in asphalt industry) systems, 2015.
- [4] Sébastien Declaye Pierre Dewallef Vincent Lemort Sylvain Quoilin, Martijn Van Den Broek. Techno-economic survey of organic rankine cycle (orc) systems, 2013.



EVALUATION ON USING WEATHER DATA FROM CITIES LISTED IN THE NBR 16401 FOR AIR CONDITIONING DESIGN IN NON-LISTED CITIES

Author: Thamires Lima da Paixão Bernardes¹ thamires-bernardes@hotmail.com
Advisor(s): Manoel Antonio da Fonseca Costa Filho¹
¹ Rio de Janeiro State University

PPG-EM Seminars: season 2019
<http://www.ppgem.uerj.br>

June, 2019

Keywords: Thermal load, Project cities, Weather data.

1 Introduction

Air conditioning systems are designed based on the thermal loads of buildings. The Brazilian standard NBR 16401 recommends that the thermal load calculations are as accurate as possible, in order to make use of lower safety factors.

Thermal load calculation accuracy depends on the quality of information available, including the weather conditions from where the building is located.

The Brazilian standard NBR 16401-1 [2] provides climatic data for 34 cities and, for other cities not listed it defines criteria to find among the cities listed, that whose climatic parameters are the closest to the project city.

This manuscript aims to enlarge the study of result evaluation of using weather data of listed cities in the Brazilian standard to calculate the thermal load of buildings located in cities not listed by it.

2 Materials and Methods

For the analysis, the thermal load of the same building was calculated in two different ways: using the recommendation of the standard and using specific weather data of the project city obtained from the DwpGen [3]. This is a web system that complies meteorological data processing criteria established by ASHRAE [4] for obtaining weather data from HVAC projects.

Due to the complexity of the thermal load calculations, since they should take into account the simultaneity occurrence of all sources of heat loads as well as the dynamic effect of the building mass, it was necessary to use the software Hourly Analysis Program (HAP) version 5.11, developed, licensed and marketed by Carrier, destined to produce the complete profile of the thermal load of a building and to analyze the energy consumption of the air conditioning system.

Ten cities of different Brazilian bioclimatic zones were

determined to compose the object of study, in order to make it more comprehensive.

The comparative criteria recommended by NBR 16401-1 [2] were used to identify which city listed has the most similar parameters to those of the project location. These criteria are: both cities must be located in the same Bioclimatic Zone (BZ) presented in NBR 15220-3 [1], have close altitudes and the same warmest and coolest months.

Following criteria defined in that standard, the corresponding cities were identified. No city listed in the standard belongs to bioclimatic zones 2 and 5, then it was necessary to identify Compatible Bioclimatic Zones (CBZ) for project cities belonging to these zones.

The calculation of thermal load was carried out in two different ways for each city of study:

- DwpGen method: The thermal load of the building was calculated based on the weather data obtained through the DwpGen web system for the project city, adopting the frequency level of 1%.
- NBR method: The thermal load was calculated based on the recommendation of NBR 16401-1. That is, the design data were those provided by the standard for the cities corresponding to the project cities, adopting the frequency level of 1%.

To evaluate the thermal load variation exclusively due to changing the building location, all internal heat sources, building envelope properties and facade orientations have remained constants.

3 Results

The results obtained were analyzed from the thermal load peak for the typical design day. The limit of 10 % of the thermal load difference was established as a decision criterion for the representativeness of the climatic parameters of the corresponding city for the design of air-conditioning systems in the project cities.

Table 1 shows the thermal load differences and the decision making regarding the adequacy of the use of weather data.

Table 1: Difference of Thermal Load between NBR and DwpGen.

Project city (BZ/CBZ)	Corresponding city (BZ)	Thermal load diference	Acceptable decision
Canela/RS (1)	Curitiba/PR (1)	7,1%	Yes
Teresópolis/RJ (2/3)	Belo Horizonte/MG (3)	12,1%	No
Santa Maria/RS (2/3)	Foz do Iguaçu/PR (3)	4,4%	Yes
Resende/RJ (3)	Londrina/PR (3)	8,2%	Yes
São Carlos/SP (4)	Brasília/DF (4)	-0,4%	Yes
Itiruçu/BA (5/6)	Goiânia/GO (6)	13,0%	No
Governador Valadares/MG (5/6)	Campo Grande/MS(6)	6,3%	Yes
Montes Claros/MG (6)	Campo Grande/MS (6)	27,3%	No
Imperatriz/MA (7)	Teresina/PI (7)	-4,0%	Yes
Ilhéus/BA (8)	Natal/RN (8)	12,5%	No

4 Conclusions

From the thermal load calculation methods presented, it was possible to evaluate, for each project city, the influence of using corresponding city weather data in the thermal load calculations.

Among the ten cities that compose the study sample, for four of them, it was verified the inadequacy of using weather data from listed cities for the design of air-conditioning systems. Among the cases of inadequacy, for 50% of them (Teresópolis and Itiruçu), there was a need to adopt the criterion compatible bioclimatic zones, since NBR 16401-1 does not list cities belonging to bioclimatic zones 2 and 5.

The NBR 16401-1 was conservative for most cases. This was acceptable in the past, however, with the current and growing concern about the operating costs of buildings, any over-sizing is undesirable. Mainly because the equipment will operate more than 99 % of the time away from the peak.

Considering the Brazilian territorial extension, it is necessary to increase the number of cities with climatic parameters listed in the standard.

Through a more representative sample of cities listed in the NBR 16401-1 standard, designers can determine listed cities with climatic parameters even closer to those of project cities. Consequently, air-conditioning designs will become more faithful to the reality of the installed plant, which will generate energy savings and savings of financial resources regarding the installation and operation of the system.

Therefore, it is necessary to revise the NBR 16401-1

standard to increase the number of cities listed, so that there is a considerable variety of cities in each Brazilian bioclimatic zone, for different altitude ranges, since these are the main parameters of influence in the thermal load calculations.

5 Acknowledgments

The authors thank to CAPES for the financial support, to INMET for providing weather data used in this work, to Carrier for the free transfer of the HAP license to UERJ and to Raama Costa Alves for developing the web system DwpGen.

References

- [1] ABNT. *Associação Brasileira de Normas Técnicas - NBR 15220-3: Desempenho térmico das edificações - Zoneamento bioclimático brasileiro e diretrizes construtivas para habitações unifamiliares de interesse social*. 2005.
- [2] ABNT. *Associação Brasileira de Normas Técnicas - NBR 16401-1: Instalações de Ar-condicionado – Sistemas Centrais e Unitários. Parte 1: Projeto das instalações*. 2008.
- [3] T. L. P. ; COSTA FILHO M. A. F. ALVES, R. C. ; BERNARDES. Web system for weather data processing to hvac design. in: 17th brazilian congress of thermal sciences and engineering, 2018, Águas de linoia - sp. proceedings of encit 2018. 2018.
- [4] ASHRAE. *American Society of Heating, Refrigerating, and Air-Conditioning Engineers – Handbook Fundamentals. Chapter.14. Climatic Design Information*. 2013.



POOL FIRE AND THERMAL RADIATION MODELING USING COMPUTATIONAL FLUID DYNAMICS

Author: Marcelo André Cordeiro da Silva¹ marceloacs@bol.com.br
Advisor(s): Norberto Mangiavacchi¹

¹ Rio de Janeiro State University

PPG-EM Seminars: season 2019
<http://www.ppgem.uerj.br>

June 18, 2019

Keywords: CFD, FDS, fire modeling, radiative heat flux.

1 Introduction

The storage of flammable liquids, such as fuels, in aerial tanks in industrial plants, logistics terminals and conveyor bases offers fire hazard caused by leakage of flammable liquid from the tank in contact with flammable vapor released with air and ambient heat, and risk of injury and death to persons due to contact with the flames and the thermal radiation emitted by the fire. The intensity of thermal radiation received from a fire can cause burns of 1st, 2nd and 3rd degrees, depending on the distance between the fire and the victim. It is necessary to analyze possible fire scenarios, calculate the safe distances between the fire and the sensitive receivers (population, residences, schools, churches, gymnasiums, etc) and compare with the admissible criteria of risk levels.

2 Methodology

This article presents a method to model and simulate pool fire and thermal radiation applying computational fluid dynamics (CFD). A fire model and simulations are presented and the radiation distances from fire are calculated to $5kW/m^2$ (capable of causing 2nd degree burns with 40s exposure) and for probability of death of 1%.

2.1 Computational tools

To do this work it was used as computational tools the the programs Fire Dynamics Simulator (FDS), Smokeview (SMV), Pyrosim and Matlab.

2.1.1 Fire Dynamics Simulator (FDS)

Fire Dynamics Simulator (FDS) is a Computational Fluid Dynamics (CFD) software of thermally driven flow [5] with large-eddy simulation (LES) and Direct Numerical Simulation (DNS) code for low-speed flows (less than 0.3 Mach) with an emphasis on smoke and heat transport from fires. FDS solves numerically Navier-Stokes equations for momentum, mass and species transport, energy transport and combustion reaction. Uses finite volume method for radiation modeling and finite

difference method for other models.

2.1.2 Smokeview (SMV)

Smokeview (SMV) is a visualization program used to display the output of FDS simulations. It's available in FDS package.

2.1.3 Pyrosim

Pyrosim is a graphical user interface program for FDS and SMV that becomes easier to built models in FDS.

2.2 Mathematical model

The FDS mathematical model are composed of hydrodynamic model, combustion model and thermal radiation model [1] [3].

Hydrodynamic model [4]:

$$\frac{\partial \rho}{\partial t} + \nabla \cdot \rho \mathbf{u} = 0 \quad (1)$$

$$\rho \left(\frac{\partial \mathbf{u}}{\partial t} + \frac{1}{2} \nabla |\mathbf{u}|^2 - \mathbf{u} \times \boldsymbol{\omega} \right) + \nabla p - \rho \mathbf{g} = \nabla \cdot \boldsymbol{\sigma} \quad (2)$$

$$\rho c_p \left(\frac{\partial T}{\partial t} + \mathbf{u} \cdot \nabla T \right) - \frac{dp_0}{dt} = \dot{q} + \nabla \cdot k \nabla T \quad (3)$$

$$p_0(t) = \rho RT. \quad (4)$$

Where, ρ is density; \mathbf{u} is the velocity vector; $\boldsymbol{\omega}$ is the vorticity; p_0 is the average pressure; \mathbf{g} is the gravity; c_p is the specific heat at constant pressure; T is the temperature; k is the thermal conductivity; t is time; \dot{q} is the volumetric heat released; R is the gas constant and $\boldsymbol{\sigma}$ is the standard stress tensor for compressible fluids.

Combustion model:

$$\dot{q}_c'' = \Delta H_o \frac{dY_o}{dZ} \rho \nabla Z \cdot \mathbf{n}; Z < Z_f. \quad (5)$$

Where, \dot{q}_c'' is the heat release rate per unit area of flame surface; ΔH_o is the energy released per unit mass of oxygen consumed, being almost constant for a wide range of fuels; \mathbf{n} is the unit normal facing outward from the fuel; Z is the mixture fraction of air and fuel; Z_f is this mixture fraction limit to combustion; dY_o/dZ is the oxygen consumption; ρ is the density; and D is the equivalent diameter of flame area.

Thermal radiation model:

$$\mathbf{s} \cdot \nabla I_\lambda(\mathbf{x}, \mathbf{s}) = \kappa_\lambda(\mathbf{x})[I_b(\mathbf{x}) - I_\lambda(\mathbf{x}, \mathbf{s})]. \quad (6)$$

Where, $I_\lambda(\mathbf{x}, \mathbf{s})$ is the radiation intensity at wavelength λ ; $I_b(\mathbf{x})$ is the source term given by the Planck function, \mathbf{s} is the unit normal direction vector and $\kappa_\lambda(\mathbf{x})$ is the spectral absorption coefficient.

2.3 Probit equation

The probability of death due to the exposure to heat radiation from fire is calculated with use of a probit function. The probit function for death due to heat radiation is given by [2]:

$$Pr = -36.38 + 2.56 \ln(Q^{2/3}t). \quad (7)$$

Where, Pr is the probit corresponding to the probability of death; $Q(W/m^2)$ is the heat radiation and $t(s)$ is the exposure time.

2.4 Accidental scenario

Two simulations to an accidental scenerario of pool fire in a containment basin due to a Diesel aerial storage tank leakage were simulated, with two different measurement methods to radiative heat flux. The models were built in FDS code using partially Pyrosim to help with complex geometries. Smokeview displayed the simulations. The radiative heat flux due to fire were measured in one simulation with measurement method I and in other with measurement method II. Measurement method I consists of 20 radiometers arranged along cartesian x and y axes with $3m$ of spacing between them and measurement method II consists of 52 radiometers arranged along 14 lines parallel to the x -axis in the distances of 1, 3, 5, 6, 8.5, 11, 15, 20, -1 , -3.5 , -6 , -8.5 , -11 , -15 and $-20m$. In each case the radiometers height $Z = 1.7m$. To each method were found the distances from fire to a radiative heat flux intensity of $5kW/m^2$ and to the probability of death of 1%. In measurement method I the FDS outputs were interpolated to give the refered distances, and in the measurement method II the FDS outputs were inputed in a Matlab code to give the refered distances and their respectives isocurves of intensity.

3 Results

The two pool fires simulations runned in FDS to simulate 40s of fire. Figure 1 shows simulation in time $t = 20s$. The probit value calculated to the probability of 1% of death was $9.8kW/m^2$.

The table 1 presents the distances found with measurement method I and II to radiative heat flux equal to $5kW/m^2$ and $9.8kW/m^2$.

4 Conclusions

The measurement method II showed to be more appropriate to measure radiative heat flux from fire. The mesh refinement in the model in FDS to generate more accurate results, must take into account the relevance

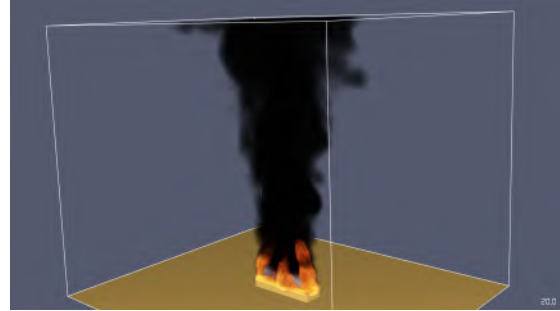


Figure 1: Pool fire simulation in $t = 20s$

Table 1: Distances from fire to radiative heat flux of $5kW/m^2$ and $9.8kW/m^2$ to measurement methods I and II

Method I		Method II	
5 kW/m ²	9.8 kW/m ²	5 kW/m ²	9.8 kW/m ²
7.5 m	5.2 m	11.0 m	9.2 m

of the improvement of the results. Other simulations should be performed to verify more results.

5 Acknowledgments

The author thank to INEA (Rio de Janeiro State Institute of Environment) to the oportunity to do this work and Thunderhead Engineering for providing Pyrosim student license free.

References

- [1] *Fire Dynamics Simulator Technical Reference Guide Volume 1: Mathematical Model*, publisher = NIST Special Publication 1018-1 - Sixth Edition, year = 2018, author = National Institute of Standard and Technology, USA.
- [2] *Guidelines for Quantitative Risk Assessment – CPR 18E Part One: Establishments – “Purple Book”*, publisher = Ministerie van VROM, Nederland, year = 2005, author = Ministerie van VROM, Nederland.
- [3] S. Hostikka, K. B. McGrattan, and A. Hamins. Numerical modeling of pool fires using les and finite volume method for radiation. In *Proceedings of the Seventh International Symposium on Fire Safety Science*, Worcester, MA, USA, 2003. International Association for Fire Safety Science.
- [4] K. McGrattan, H. R. Baum, and R. G. Rehm. Large eddy simulations of smoke movement. *Fire Safety Journal*, No. 30 (1998), pages 161–178, 1997.
- [5] U. M. Niazi, M. S. Nasif, M. B. Muhammad, and M. Imran. Modelling of pool fire and injury prediction considering different wind speeds and directions in offshore platform. *ARPN Journal of Engineering and Applied Sciences*, 11:13000–13005, 2016.



ANALYSIS OF MECHANICAL CHARACTERISTICS OF A POLYMER-MATRIX COMPOSITE REINFORCED WITH RESIDUES FROM BRAZILIAN COAL-FIRED THERMAL POWER PLANT

Author: Diego de Lima Gomes; (GOMES, D.L.)¹ diego.lima@uerj.br
Advisor(s): Marilia G. Diniz¹

¹ Rio de Janeiro State University

PPG-EM Seminars: season 2019
<http://www.ppgem.uerj.br>

Jun 25, 2019

Keywords: Industrial residues, fly ash cenospheres, composite, epoxy resin.

1 Introduction

The use of epoxy resin in composite has been studied for the reason of low cost, but the application of some polymers is limited by mechanical characteristics such as low impact strength, tensile and fatigue, dimensional stability and abrasion resistance [5] [7]. Generally, materials such as fillers are used which reinforce the structure to obtain better mechanical strength, in many engineering applications [4]. These fillers are chosen according to the application and mode of manufacture, they can be fibers, natural materials or particles such as ceramic powders [3].

Researches in the civil sector already uses ash as a part of cement additives and ceramics production, bricks and block making, as a strong, stable, fire-resistant and recyclable material [8]. Other studies evaluate the ash synthesis to the use of adsorbent filters for combustion gases, noise barriers, fire panels, among other purposes [1].

Materials used as filler or reinforcement in composites are generally inert materials used to improve mechanical properties, reduce the weight and costs of the material and in some cases modify the processability. Therefore, this work contributes to the minimization of discards of industrial waste, making possible use of fly ashes in industrial processes [6].

2 Materials and Methods

2.1 Fly ash characterization

A Sample of fly ash obtained by the burning of mineral coal in a thermoelectric plant located in southern Brazil were used as reinforcement and dimensional filling of a polymer matrix composite in this work. Test specimens were produced using a thermosetting (epoxy resin and hardener).

The granulometric distribution of the particles were carried out using the sieving method and the fractions classified according to the Tyler sieve series (100 to

635) mesh were obtained.

High resolution images of ash particles, was performed by scanning electron microscope (SEM) with secondary electron detector (SEI).

2.2 Preparation of composite

The epoxy resin and hardener were mixed together in a ratio of 10:1 by weight. This mixture was gently stirred to avoid bubbles in the resin. The unmodified fly ash in micron size particles were then slowly added at desired concentrations from 30 % wt. and mixed. The FA/epoxy composite was conventionally cured at room temperature (23 ± 2 C). The mould set up was kept in room temperature for 24 hrs.

3 Results

The analysis by microscopy techniques allowed the study of the structure and morphology of the particles of fly ash particles used in the reinforcement of a polymer matrix.

The morphological aspect of the particles that compose the ashes was predominantly spherical, of varied diameters and a few particles of irregular forms. For good reinforcement the particle size should be finer and should have higher surface area.

Using scanning electron microscopy, the particle size distribution of very fine particles of fly ash were observed as shown in Fig. 1. The granulometric distribution by sieving revealed that 80% of the material is of particle size less than 90 microns (170 Tyler mesh) Fig. 2.

The chemical composition of fly ash determined by atomic absorption spectrophotometry (AAS) reveals the abundant presence of silica as the main constituent along with alumina and traces of other oxides.

The distribution of the particles in the polymer matrix was homogeneous Fig. 3. The mechanical behavior is directly associated to the inorganic filler of composites. Observation of particles by SEM with different magnification was used to analyze shape and cohesion with the matrix.

The addition of fly ash particles may improve the

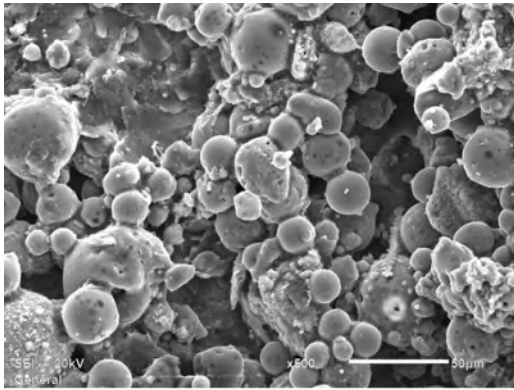


Figure 1: Aspect of coal fly ash particles. SEM, 500x.

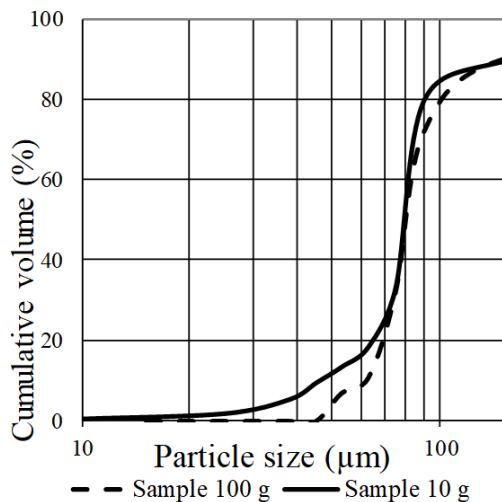


Figure 2: Particle size distribution of fly ash.

mechanical and thermal properties of FA/epoxy composite [8]. It is expected that the addition of inorganic fillers can act as physical interlocking points in the cured organic matrix [2], which allows to prolong the use in the industrial environment.

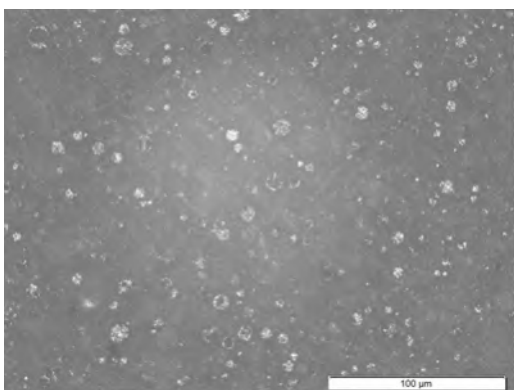


Figure 3: Microstructure of the polymer-matrix composite.

4 Conclusions

The use of mineral fillers may contribute as an option to reinforcement in polymers, contributing to the in-

crease in wear resistance in tribological applications and dimensional stability, as well as to minimize mass and design flexibility.

The use of ash will make it possible to reduce costs, since this raw material is a residue of coal-fired thermoelectric plants, offering a nobler destination for this waste that is currently discarded in the environment or reused by the cement industry.

5 Acknowledgments

The authors acknowledge the support from the Brazilian funding agency CNPq.

References

- [1] Ximena Castillo, Jaime Pizarro, Claudia Ortiz, Héctor Cid, Marcos Flores, Els De Canck, and Pascal Van Der Voort. A cheap mesoporous silica from fly ash as an outstanding adsorbent for sulfate in water. *Microporous and Mesoporous Materials*, 272:184 – 192, 2018.
- [2] Ping Chen, Yuan Wang, Jianchao Li, Hui Wang, and Lei Zhang. Adhesion and erosion properties of epoxy resin composite coatings reinforced with fly ash cenospheres and short glass fibers. *Progress in Organic Coatings*, 125:489 – 499, 2018.
- [3] Carlos D. Garcia, Kiran Shahapurkar, Mrityunjay Doddamani, G.C. Mohan Kumar, and Pavana Prabhakar. Effect of arctic environment on flexural behavior of fly ash cenosphere reinforced epoxy syntactic foams. *Composites Part B: Engineering*, 151: 265 – 273, 2018.
- [4] Anjani R.K. Gollakota, Vikranth Volli, and Chi-Min Shu. Progressive utilisation prospects of coal fly ash: A review. *Science of The Total Environment*, 672: 951 – 989, 2019.
- [5] N. H.Arani, W. Rabba, and M. Papini. Solid particle erosion of epoxy matrix composites reinforced by Al_2O_3 spheres. *Tribology International*, 136:432 – 445, 2019.
- [6] James C. Hower, John G. Groppo, Uschi M. Graham, Colin R. Ward, Irena J. Kostova, Mercedes M. Maroto-Valer, and Shifeng Dai. Coal-derived unburned carbons in fly ash: A review. *International Journal of Coal Geology*, 179:11 – 27, 2017.
- [7] Hitesh Kesarla, K. Rohit, Ajinkya Mohod, Shekhar Tanji, Onkar Mane, and G. Venkatachalam. Study on tensile behavior of fly ash reinforced hybrid polymer matrix composite. *Materials Today: Proceedings*, 5(5, Part 2):11922 – 11932, 2018.
- [8] Hongyu Zhou and Adam L. Brooks. Thermal and mechanical properties of structural lightweight concrete containing lightweight aggregates and fly-ash cenospheres. *Construction and Building Materials*, 198:512 – 526, 2019.



ELECTRIC VEHICLE WITH PHOTOVOLTAIC POWER SOURCE

Author: Juan Carlos Azeredo Coutinho¹
Advisor(s): Luiz Artur Pecorelli Peres¹

azeredcoutinho@hotmail.com

¹ Rio de Janeiro State University

PPG-EM Seminars: season 2019
<http://www.ppgem.uerj.br>

July 12, 2019

Keywords: Electric vehicle, photovoltaic cells, algorithm.

1 Introduction

The present work has as objectives: the analysis and study of the conversion of an internal combustion vehicle to electric traction in two different situations. The first situation the original gearbox of the vehicle is maintained. In the second situation it is dismissed. In both situations the conversion performed presents a method for using photovoltaic cells in order to increase the autonomy of the traction batteries used. In this work, knowledge related to traction mechanics, photovoltaic cells, electrochemical traction sources and all the necessary system for the development of an electric vehicle with greater energy efficiency and lower consumption are used.

This study sized the conversion of the internal combustion system of a Towner (mini van category) vehicle for electric traction including the alternating current motor coupled to a frequency inverter that is provided with regenerative braking. As a result, there was 10

This development included the construction of a program in Matlab that allows to obtain the necessary values for the choice of an equivalent electric motor in the market in substitution to the original internal combustion engine.

Figure 1 shows the diagram of the proposed car for a better knowledge of the project.

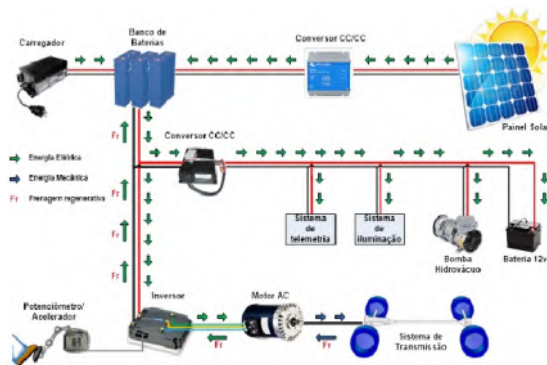


Figure 1: Diagram of the electric photovoltaic car.

2 Methodology

The vehicle chosen for conversion is the Towner (mini van category) model from Asia Motors. Its choice was motivated by its enormous versatility and being a small vehicle with a capacity of up to seven passengers, which makes it a great option for urban transportation in big cities.

For the conversion, initially the space available for the engine and the battery bank was observed. Then, based on the mass of the vehicle, two important conditions of displacement were observed: the start, when the vehicle will have to overcome the inertia assuming the highest slope angle in the course and the maximum speed that the vehicle intends to obtain in the plan.

Mathematical simulations were used to predict extreme system operating conditions: torque required for the vehicle to overcome the increased angle of the course to be performed and the behavior of the system when the vehicle reaches its maximum speed on the wheels. These conditions allow you to define the required torques for each of the conditions presented, and how to choose the most suitable electric motor available on the market.

After the theoretical calculations of the tensile strength with its components, wheel and motor torques, wheel rotation, motor rotation, wheel and motor angular velocity, and engine power, a program was created in Matlab mathematical software. With the program done, see Figure 2, it is possible to enter the data of a common vehicle and obtain the values necessary to choose an electric motor equivalent to the MCI of the vehicle.

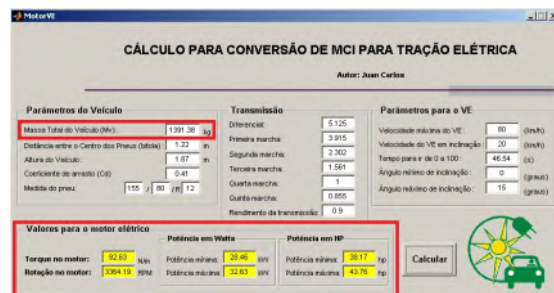


Figure 2: Program for calculating the conversion of MCI to electric traction.

With the values of the yellow axes of figure 2, the

assembly set is supplied by the AC50 motor, which provides 67.99 HP peak with 150 N/m maximum torque, and the Model 1238R inverter. -7601 of 96v 650A.

Having chosen the engine, the Automobiles - Performance Analysis of Motor Vehicles program was used, see Figure 3.

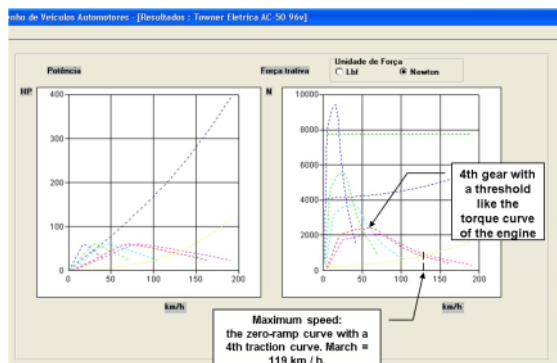


Figure 3: Screen with engine performance charts in each gear.

After the performance analysis, it can be seen from the graphs in Figure 4 that the chosen motor perfectly meets the design.

For the design of the battery bank and the autonomy of the vehicle, a small test cycle was used, Figure 5. This cycle travels a distance of 500 meters, at a maximum speed of 50 km / h, with a consumption of 0.138 kWh and using the energy generated by regenerative braking this consumption drops to 0.125 kWh, generating savings of around 10%.

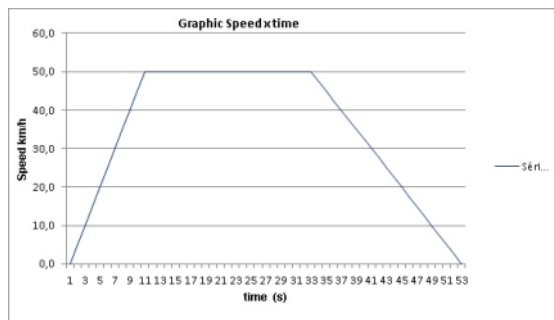


Figure 4: Test cycle, velocity vs. time graph.

The lithium-ion battery of 3.2v by 180 Ah was chosen because of the high energy density. The inverter has a power range of 96v to 108v, which necessitates a serial connection of 32 batteries, resulting in a bank of 102.4v of 180Ah batteries that will supply 18.43 kWh. On top of this value, it is necessary to apply a safety margin due to the energy consumption that will happen due to the installed electrical devices for the various auxiliary systems: lighting, signaling, vacuum pump for braking etc. For this safety margin, it will be adopted for the amount of energy available in the battery bank, for the purpose of calculating vehicle autonomy 80% of it. The new value will be 14745.6 Wh.

Using the data obtained in the test cycle, we can esti-

mate the autonomy of 58.98 km. For greater accuracy it would be necessary to calculate a cycle of tests with a greater variety of paths in order to make urban use as faithful as possible.

Knowing the available size of the 2000x790 mm ceiling and the cell data in Table 1, we can distribute the cells as follows: 12 columns of 5 cells each, forming a total of 60 cells connected in series, as shown in Figure 6.

CHARACTERISTICS OF THE CELLS BY UNIT	
Tension	0,5 volts
Maximum Current	7,6 Amperes
Maximum power	3,8 watts
Size	156 mm x 156 mm
Lifespan	over 25 years
Average Efficiency	18 a 20%
Weight	10 grams
Weight	Silicio Policristalino

Figure 5: Photovoltaic cell data.

With the association of 60 cells in series we will have a module of 30 volts by 7.6 amperes, totaling 228 watts.

To theoretically estimate the performance of the above module, we calculate the panel at its maximum power and at 80% of its power.

The simulation will be based on an exposure of 6 hours a day to the sun, which would be a range of higher incidence of solar rays.

Figure 6: Illustration of Towner with the photovoltaic module.

With 100% we have 228 watts for 6 hours with a total of 1368 watts day, autonomy of 5,472 km, which is 9.277% battery bank autonomy;

With 80% we have 182.4 watts for 6 hours with a total of 1094.4 watts day, autonomy of 4,377 km, which represents 7.42% of battery bank autonomy.

3 Conclusions

The work confirms the feasibility of dispensing the gearbox, as shown in Figure 4, the graph achieves the torque and speed compatible with the original gear characteristics in gear where the gear ratio is 1 to 1, and the use of a modulus photovoltaic system to increase the autonomy of an electric vehicle. It has also been seen that regenerative braking can give a 10% gain by reusing the energy that would be lost as heat in braking.



APPLICATION OF THE CHARACTERISTIC FUNCTION METHOD TO OBTAIN THE NON-LINEAR INTEGRAL TRANSFORM FOR AT-INSAR PHASE SPECTRUM

Author: Leonardo Paiva Ferreira da Costa¹ cardano.l@hotmail.com
Advisor(s): Luiz Mariano Carvalho¹

¹ Universidade do Estado do Rio de Janeiro

PPG-EM Seminars: season 2019
<http://www.ppgem.uerj.br>

July 12, 2019

Keywords:

AT-INSAR, interferometry, transform of the phase spectrum.

1 Introduction

The complexity of the imaging mechanisms made it difficult for many years to validate quantitative measurements of the surface wave spectrum of SAR images. A subsequent problem occurs when the goal is inverting the SAR image spectrum to obtain wind-generated wave spectra. The mapping process, because it's nonlinear, admits that a single SAR spectrum is able to map many wave-generated wave spectrum. In [2] it has been shown to be possible by an iterative process involving additional information obtained by external means, a way of obtaining a single mapping and consequently obtaining an unique relationship between SAR image spectrum and wind generated wave spectrum. This particular transform was named Hasselmann's transform [1][2]. This transform is relative to the amplitude of the wave spectrum and in article [3] a new transform was derived, based on the phase difference of the wave spectrum. This new transform is derived from interferometry technique and requires the use of two antennas positioned in the flight direction or at least is obtained using two different orbits to calculate the phase difference .

2 Application of the characteristic functions method

The Fourier transform of the AT-INSAR (along-track interferometric synthetic aperture radar) phase image function is defined as

$$I_P(\mathbf{k}) = \frac{kB}{2\pi^2V} \int \exp(-j\mathbf{k} \cdot \mathbf{x}_0) h(\mathbf{x}_0) d\mathbf{x}_0. \quad (1)$$

The AT-INSAR phase spectrum transform is obtained as

$$\langle I(\mathbf{k})_P I^*(\mathbf{k}')_P \rangle = P_P(\mathbf{k}) \delta(\mathbf{k} - \mathbf{k}'), \quad (2)$$

from the article [3]

$$P_P(\mathbf{k}) = \left(\frac{kB}{\pi V}\right)^2 \int \exp(-\mathbf{k} \cdot \mathbf{r}) \langle h(\mathbf{x}_0 + \mathbf{r}) h^*(\mathbf{x}_0) \rangle d\mathbf{r}, \quad (3)$$

where

$$h(\mathbf{x}_0) = [u_r(\mathbf{x}_0) \left(1 + \frac{R}{V} u'_r(\mathbf{x}_0)\right) \exp\left(\frac{-jkR}{V} u_r(\mathbf{x}_0)\right)], \quad (4)$$

and, $u_r(\mathbf{x}_0)$ means the orbital velocity of the back-scattered element on the surface, R is the distance between the target and the platform carrying the SAR, V is the platform's velocity. To deduce the non-linear integral transform for the AT-INSAR phase spectrum it's necessary calculating

$$\langle h(\mathbf{x}_0 + \mathbf{r}) h^*(\mathbf{x}_0) \rangle, \quad (5)$$

and for this, we'll use the characteristic function method described in [4] and applied by [3]. Defining the characteristic function

$$M(k_1, k_2) = \exp(j\mathbf{t} \cdot \boldsymbol{\mu} - \frac{1}{2} \mathbf{t}^t \boldsymbol{\Sigma} \mathbf{t}), \quad (6)$$

where the Gaussian vector it's defined through the random variables $\xi(\mathbf{x})$ and $\xi(\mathbf{x} + \mathbf{r})$. The expected value $\boldsymbol{\mu}$ is considered zero, j is the complex unity, the vector $\mathbf{t} = (k_1, k_2)$, and the co-variance's matrix is defined as

$$\boldsymbol{\Sigma} = \begin{pmatrix} c_{11} & c_{12} \\ c_{12} & c_{11} \end{pmatrix}$$

where $c_{11} = \langle \xi(\mathbf{x})^2 \rangle$ and $c_{12} = \langle \xi(\mathbf{x} + \mathbf{r}) \xi(\mathbf{x}) \rangle$. Making these calculations, we obtain

$$M(k_1, k_2) = \exp \left[-\frac{1}{2} (k_1^2 c_{11} + 2k_1 k_2 c_{12} + k_2^2 c_{11}) \right] \quad (7)$$

Rewriting equation (5) in function of the characteristic function and doing some trivial, but laborious calculations, and replacing $\xi(\mathbf{x})$ for $u_r(\mathbf{x}_0)$, $k_1 = \frac{k_x R}{V}$ and $k_2 = -\frac{k_x R}{V}$ ¹ where k_x is the wavenumber's azimuthal component, we obtain the final transform which

¹The main reason that use only the component k_x , is that [4] states that only the azimuthal component matters.

is used to recover the wave spectrum $F(\mathbf{k})$ inverting $P_P(\mathbf{k}) = T(F(\mathbf{k}))$, where T is the transform calculated in equation (8).

3 Results

$$\begin{aligned}
 P_P^S(\mathbf{k}) &= \left(\frac{k_x B}{\pi V} \right)^2 \int d\mathbf{r} \exp(-j\mathbf{k} \cdot \mathbf{r}) \\
 &\quad \times \exp \left[\left(\frac{k_x B}{V} \right)^2 (f^u(\mathbf{r}) - f^u(\mathbf{0})) \right] \\
 &\quad \times \left[f^u(\mathbf{r}) + \left(\frac{k_x B}{V} \right)^2 (f^u(\mathbf{r}) - f^u(\mathbf{0}))^2 \right] \\
 &\quad \times \left(1 - \frac{\partial^2 f^u(\mathbf{r})}{\partial \mathbf{r}^2} \right) \left(\frac{k_x R}{V} \right)^2 + 2j \left(\frac{k_x B}{V} \right) \\
 &\quad \times \left(\frac{\partial f^u(\mathbf{r})}{\partial \mathbf{r}} \right) \left[2f^u(\mathbf{r}) - f^u(\mathbf{0}) + \left(\frac{k_x R}{V} \right)^2 (f^u(\mathbf{r}) - f^u(\mathbf{0}))^2 \right] \\
 &\quad - \left(\frac{R}{V} \right)^2 \left(\frac{\partial f^u(\mathbf{r})}{\partial \mathbf{r}} \right)^2 \left[1 + \left(\frac{k_x R}{V} \right)^2 (3f^u(\mathbf{r}) - \right. \\
 &\quad \left. - 2f^u(\mathbf{0})) + (f^u(\mathbf{r}) - f^u(\mathbf{0}))^2 \left(\frac{k_x R}{V} \right)^4 \right], \quad (8)
 \end{aligned}$$

where ω means angular frequency.

$$f^u(\mathbf{r}) = \langle u_r(\mathbf{x}_0 + \mathbf{r}) u_r(\mathbf{x}_0) \rangle \quad (9)$$

$$f^u(\mathbf{r}) = \frac{1}{2} \int (|T_k^u|^2 F(\mathbf{k}) + |T_{-k}^u|^2 F(-\mathbf{k})) \exp(j\mathbf{k} \cdot \mathbf{r}) d\mathbf{k}. \quad (10)$$

With the range velocity transfer function

$$T_k^u = \omega \left(\sin \theta \frac{k_l}{|k|} + j \cos \theta \right). \quad (11)$$

Simplifying the equation 8 like in [3], we obtain a quasi-linear transform equation 12

$$\begin{aligned}
 P_{Pqt}^S(\mathbf{k}) &= \frac{\exp(-k_x^2 R^2 V^{-2} f^u(\mathbf{0}))}{2} \times \\
 &\quad (|T_k^u(\mathbf{k})|^2 F(\mathbf{k}) + |T_k^u(-\mathbf{k})|^2 F(-\mathbf{k})), \quad (12)
 \end{aligned}$$

and that quasi-linear transform carries some relevant information of the original transform.

4 Conclusions

- The quasi-linear transform of amplitude present in [2] is similar to the quasi-linear transform of phase, with the exception of the $f^u(\mathbf{0})$
- Both transforms depend on the transfer functions, and dependents of the modulation effects occurring on the surface.
- The AT-INSAR integral transform for the phase spectrum is less dependent on the modulating effects than the integral transform for the amplitude spectrum.
- For future studies, it is necessary to analyze the mathematical conditions to apply this theory.
- In article [3], it is suggested that this new transform has the potential to estimate the velocity field of the ocean's currents.

5 Acknowledgments

- I'd like to thank André Luiz Cordeiro dos Santos, Felipe Marques dos Santos and my advisor Luiz Mariano Carvalho for all the help needed developing this dissertation.
- I'd also like to thank CAPES for the financial support.

References

- [1] André Luiz Cordeiro dos Santos. *Recuperação do espectro direcional de ondas oceânica com o uso de radar de abertura sintética*. PhD dissertation, Universidade do Estado do Rio de Janeiro, 2015.
- [2] Klaus Hasselmann and Susanne Hasselmann. On the nonlinear mapping of an ocean wave spectrum into a synthetic aperture radar image spectrum and its inversion. *Journal of Geophysical Research: Oceans*, 96(C6):10713–10729, 1991.
- [3] Yijun He and Werner Alpers. On the nonlinear integral transform of an ocean wave spectrum into an along-track interferometric synthetic aperture radar image spectrum. *Journal of Geophysical Research: Oceans*, 108(C6), 2003.
- [4] Harald Krogstad. A simple derivation of hasselmann's nonlinear ocean-synthetic aperture radar transform. *J. Geophys. Res.*, 97:2,421–2,425, 02 1992. doi: 10.1029/91JC03010.



ASSESSMENT OF THE DYNAMIC RESPONSE AND FATIGUE ANALYSIS OF FLOORS SUBJECTED TO ACTION OF MECHANICAL EQUIPMENT

Author: Álvaro Eduardo do Amaral Menezes Júnior¹
Advisor(s): Francisco Soeiro¹ and José Guilherme¹

alvaro.eduardo@ifb.edu.br

¹ Rio de Janeiro State University

PPG-EM Seminars: season 2019
<http://www.ppgem.uerj.br>

Oct 29, 2019

Keywords: FEM, Dynamic Structure, Fatigue analysis.

1 Introduction

This paper aims the study of the dynamic structural response and evaluates the fatigue response in terms of its structural service life of floors when subjected to the loading action of mechanical equipment (condenser). The numerical modelling of the studied composite floor was performed by the ANSYS program, according to the Finite Element Method (FEM). The applied loads were simulated based on harmonic dynamic actions related to the dynamic loadings imposed by the equipment on the structure. The methodology and the procedures presented in the design codes were used to evaluate the floor fatigue response. The conclusions are focused on the evaluation of the service life response of steel-concrete composite floor service life, when subjected to the dynamic actions induced by the mechanical equipment.

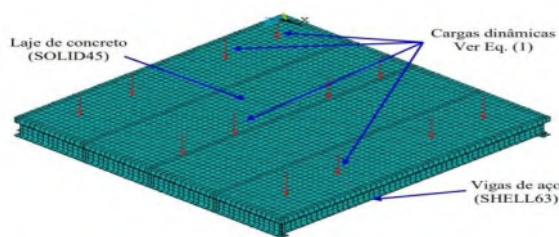


Figure 1: FEA Model of steel-concrete floor.

2 Steel-concrete composite floor

The material used for this study is a steel beam ASTM A572 Gr. 50 ($f_y = 345$ MPa) and concrete slab ($f_{ck} = 25$ MPa). The main and secondary beams are composed by W360 x 32,9 and W250 X 28,4 channels. The investigated structural system is based on a steel-concrete composite floor with dimensions of 5m x 5m, a total area of 25 m² and 10 mm of thickness. The structure is a technical floor where mechanical equipment is installed. The equipment used in this research is 38 GPa condenser unit (Weight 490 Kgf, Frequency: 16 Hz)

[2]. The static forces originate from weight of its own structure, its coat and equipment. The dynamic forces considered are related to the harmonic dynamic actions from equipment rotor and its transient response is given by Equation 1:

$$F(t) = F_0 \sin(\omega t) = M\omega R \sin(\omega t) \quad (1)$$

Where F_0 is the amplitude harmonic of force [$F_0 = M \omega e$]; M is the rotor mass; ω is excitation frequency ($\omega = 100,53$ rad/s ou $f = 16$ Hz); e is eccentricity; R ($R = \omega e$) is the numerical value of the selected balance quality grade, ($R = 2,5$ mm/s) [5]; and t represent the time [3].

Since the manufacture does not report the value of rotor mass, two possibilities were adopted for rotor mass. The first one was considering the mass of equipment being the same as rotor. The second was adopting 18% of equipment mass, according to Petrobras Standard, N-1848 [4]. The analyzes were simulated with 2,4 and 6 equipment.

3 Dynamic structural analysis

The analysis was realized by use of Finite Element Method (FEA) software ANSYS [1]. The structural model of the concrete slab floor was generated with SOLID45 with a equivalent mesh to 3074 elements. Similarly, the model of the steel beams used SHELL63 and performed 2677 elements. The numerical model had 8700 nodes, according to Fig. 1.

The forced vibration analysis, in the time domain, based on the equipment position (2, 4 and 6 condensers) represents a key point in obtaining natural frequency and vibration modes.

The dynamic actions was applied in the vertical direction, on the support position of the concrete slab. The dynamic loads from the equipment was applied according to the Eq. 1 and the Newmark method were used for the numerical integration of the dynamic equilibrium equations with a Δt equivalent to 10 s.

4 Results

The natural frequencies (eigenvector) and vibration modes (eigenvalues) were obtained from a free vibration analysis (modal analysis) with ANSYS (2012) software. Fig. 2 shows the first four results of this analysis. Checking the values of the natural frequencies of the structure. It is possible to note that the first one has an excitation frequency of 16 Hz, the same as the first natural frequency of floor flexion, thus a resonance.

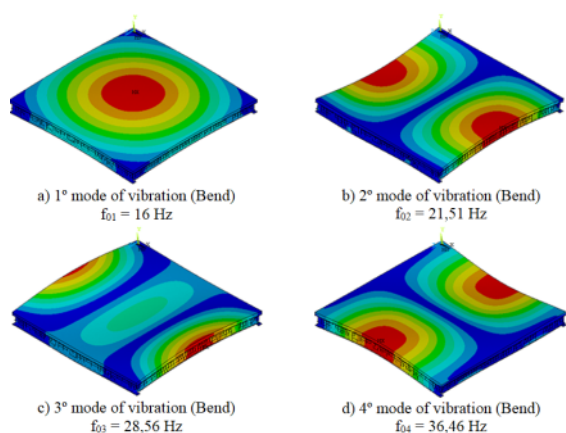


Figure 2: Mode of Vibration.

The dynamic structural response of the floor was obtained by applying static and dynamic loading from the condensing units. It was considered a structural damping ratio equal to 1.5% [3]. The node chosen to analyze the dynamic response of the floor was the one where the maximum effects occurred, located in the middle of the central secondary beam (W250 x 28.4), See Fig. 3. Table 1 presents the dynamic response results of the floor, in the permanent phase of the response, in the section where the maximum values of displacements and stresses.

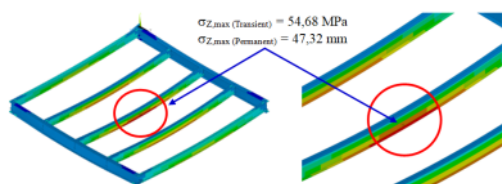


Figure 3: Maximum floor tension.

Table 1: Vertical translational displacements (U_y) and maximum stresses (σ_Z).

Dynamic Loading Cases	U_y (mm)	σ_Z (MPa)
6 condensers: 100% of total mass of equipment	4,18 mm	54,68 MPa
6 condensers: 18% of total mass of equipment	3,80 mm	47,32 MPa
4 condensers: 100% of total mass of equipment	3,95 mm	49,38 MPa
4 condensers: 18% of total mass of equipment	3,75 mm	46,76 MPa
2 condensers: 100% of total mass of equipment	3,94 mm	49,29MPa
2 condensers: 18% of total mass of equipment	3,67 mm	46,75MPa

To determine the service-life due to fatigue and cumulative damage it is necessary to obtain the variation of stress that happens on the structure during the period of equipment's use. Fatigue analysis was performed following the classical methodology to evaluate fatigue damage in structures due to effects caused by variable amplitude loads, based on the use of SN-type curves and the Palmgren-Miner linear damage rule and counting algorithm, Rainflow cycle [6]. The Eurocode Standard (2003) and a structural detail of the contour weld type, referring to class 63 was used. The results are shown in Tab. 2.

Table 2: Useful Life according Eurocode 3

$\Delta\sigma$ (MPa)	N cycles	(%)	Eurocode 3 (Limit 120 years)	
			Ni	ni/Ni
Six condensers: 100% of total mass of equipment				
13,09	23.5	49	223965467	0.004418
13,10	23.5	49	223452960	0.004428
13,12	0.5	1	222432629	0.000095
$\Delta\sigma_{max}$ 13.12	\sum 47.5	\sum 100	Dano (D)	0.008940729
			Service life (T = 1/D)	112 years
Six condensers: 18% of total mass of equipment				
2.25	0.5	1	44101407036	0,0000005
2.26	2.5	5	43518576648	0,0000024
2.27	44.5	94	42945971190	0,0000436
$\Delta\sigma_{max}$ 2.27	\sum 47	\sum 100	Dano (D)	0,008940729
			Service life (T = 1/D)	21.494

5 Conclusion

Based on the results presented in Tab. 2, it was verified that when the harmonic dynamic load is calculated based on the total mass value of the equipment, the structural system does not meet the design and fatigue verification limit proposed by Eurocode (2003). For this reason, N-1848 Standards recommends structure designers to consider that rotors have a mass equal to 18% of the total mass of the equipment, in the absence of technical information about mechanical equipment. Thus, observing the service-life values of the analyzed structure, presented in Table 2, it is clear that the structural system meets the design and fatigue limit proposed by Eurocode 3 (2003) with a with a considerable margin .

References

- [1] Ansys. Swanson analysis systems - theory reference (r.12.1). Technical report, 2010.
- [2] Carrier. Cat. técnico 38 gpa. multisplit alta capacidade. condensadora. Technical report, 2009.
- [3] R.W. Clough and J. Penzien. *Dynamics of Structures*. McGraw-Hill Inc, 2003.
- [4] Petrobrás. N-1848: Projeto de fundações de máquinas. Technical report, 2008.
- [5] Álvaro Eduardo de Menezes Amaral Júnior. *Análise dinâmica e verificação à fadiga de pisos mistos (aço-concreto) submetidos à ação de equipamentos mecânicos (Em desenvolvimento)*. Mestrado, UERJ, RJ, 2019.



ANALYSIS OF AIR CIRCULATION AND HYGROTHERMAL BEHAVIOR OF THE UNIVERSE MUSEUM (GÁVEA PLANETARIUM)

Author: André Patrocínio de Castro¹ fcandre23@gmail.com
Advisor(s): Manoel Antônio Fonseca da Costa Filho¹

¹ Rio de Janeiro State University

PPG-EM Seminars: season 2019
<http://www.ppgem.uerj.br>

Dec 03, 2019

Keywords: CFD, Ansys Fluent, Thermal Comfort.

1 Introduction

In the last two decades Computational Fluid Dynamics (CFD) models have been increasingly used for the calculation of airflow velocities and temperatures in indoor environments for the evaluation of comfort conditions, smoke conditions and air quality [1]. A significant number of scientific papers exists dealing with the application of CFD models in various complex indoor environments, such as museums [2] and Mosque [3]. This work demonstrates the application of a CFD model to calculate airflow speeds and temperatures in a very complex architecture (Gávea Planetarium), where the input data were obtained from ARAGÃO, 2015; and COSTA FILHO et al, 2015. The chosen day was May 12, 2014, time 12:28:20, the period of the day when the highest insolation rate occurred, which was a sunny day with no clouds as shown in the illustrations in COSTA FILHO et al. (2015). The calculated speeds and temperatures were used to determine the main thermal comfort indices Predicted average vote (PMV) and Predicted percentage of dissatisfied (PPD) [4]; these were later used for the evaluation of the thermal conditions of the Planetarium.

2 Materials and Methods

2.1 CFD Model

There are three main types of CFD methods:[5] Direct Numerical Simulation (DNS), Large Eddy Simulation (LES) and [6] Reynolds Averaged Navier–Stokes (RANS). A short presentation of these methods can be found in Stamou and Katsiris [6]. These methods are employed in various efficient computer codes, which are most frequently used for indoor CFD calculations, such as PHOENICS, FLUENT and CFX. In the present work, the version ©16.5 of the computer code Fluent was used.

2.2 The Turbulence Model

The analysis was performed considering an incompressible monophasic fluid (air), in a steady flow. The tur-

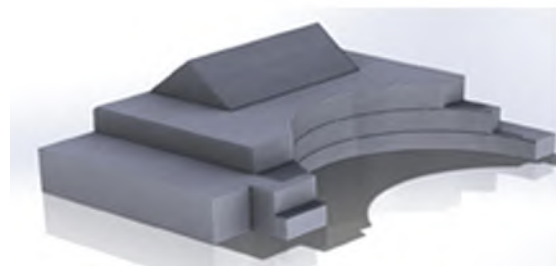


Figure 1: Planetarium internal volume

Table 1: Mesh characteristics

Number of cells	7.625.434
Number of nodes	1.408.539
Skewness	Max=0.973
Mesh type	tetrahedral

bulence model chosen was $\kappa - \epsilon$. The solution used was based on pressure, which solves the speed field from the momentum and mass conservation equation, and the temperature field from the energy equation.

2.3 Geometry

For the 3D modeling of the control volume to be analyzed, the SolidWorks modeling R©2013 tool was used, view in figure 1.

2.4 Meshing

The mesh was generated with the software's default feature, refined in the regions of interest (Inlets, Outlets, Pillars and Ducts), due to computational limitation. The mesh generation time for a high number of cells, due to the size of the geometry, was relatively short. Table 1 presents the main characteristics of the refined mesh:

2.5 Boundary Condition

The boundary conditions inserted in AnsysFluent were removed from the design of the air conditioning system, provided by the Planetarium or directly obtained from the experimental data [7].

Table 2: Shows the materials used and their properties.

Material	Dens. (kg/m^3)	Spec.Heat ($J/kg.K$)	Thermal C. ($W/m.K$)
Air (15°C)	1.22	1,006.43	0.02
Concrete	2300	1000	1.75
Galv.Steel	7800	460	55
Glass	2500	840	1

Table 3: Calculated values of PMV and PPD

Floor	T_{min}	T_{max}	PMV	PPD
2m	21.0°C	24.7°C	-2.02	77.59%
4m	22.3°C	29.2°C	-0.39	8.16%
7m	21.8°C	60.9°C	1.45	48.35%
10m	28.7°C	56.9°C	5.95	100%

2.6 Thermal Comfort

ISO 7730 [4] presents methods for predicting the general thermal sensation and degree of discomfort (thermal dissatisfaction) of people exposed to moderate thermal environments. It enables the analytical determination and interpretation of thermal comfort using calculation of PMV (predicted mean vote) and PPD (predicted percentage of dissatisfied) and local thermal comfort criteria, giving the environmental conditions considered acceptable for general thermal comfort as well as those representing local discomfort. The PMV is an index that predicts the mean value of the votes of a large group of persons on the 7-point thermal sensation scale [4]. The PMV can be determined using Eq. (1)

$$PMV = [0.303 \exp(-0.036M) + 0.028] \cdot L \quad (1)$$

The PPD is an index that establishes a quantitative prediction of the percentage of thermally dissatisfied people who feel too cool or too warm.[4] The predicted percentage dissatisfied (PPD) is a function of PMV and is given by equation (2),

$$PPD = 100 - 95 \exp(-0,0335PMV^4 - 0,2179PMV^2) \quad (2)$$

3 Results

The simulation results were satisfactory since they converged to the experimental data. From this, the study allowed us to analyze the thermal behavior of the interior of the planetarium through the temperature and air velocity fields, indicating possible points of thermal discomfort. We can see in figure 2.

4 Conclusions

The results obtained with the CFD at the Planetarium showed that the temperature gradient between the ground floor and the top floor is very high, which severely influences the thermal sensation of visitors. The calculated values of PMV and PPD (Table 3) showed that the thermal conditions very abruptly as

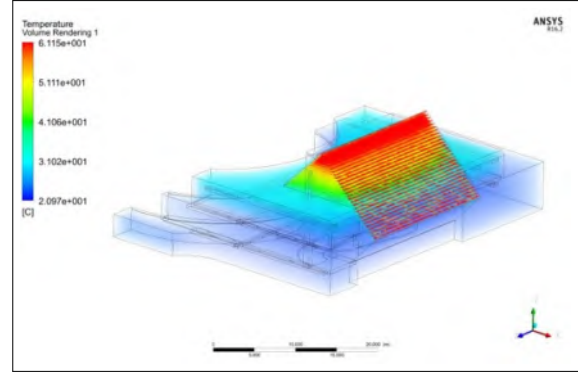


Figure 2: Temperature field

the person starts the transition between floors; only the region close to 4m in height is in a comfortable condition since less than 10% is dissatisfied (PPD). In the region below 4m, we find a high percentage of people with a feeling of COLD, and in the region where the hot air is stagnant, above 7m, it is quite uncomfortable, as shown by the distribution of the airflow lines [8].

References

- [1] A. I. Stamou and I. Katsiris, "Evaluation of thermal comfort in galatsi arena of the olympics "athens 2004" using a cfd model," *Applied Thermal Engineering*, vol. 28, no. 10, pp. 1206 – 1215, 2008.
- [2] K. Papakonstantinou and C. Kiranoudis, "Computational analysis of thermal comfort: the case of the archaeological museum of athens," *Applied Mathematical Modelling*, vol. 24, no. 7, pp. 477 – 494, 2000.
- [3] H. M. Kamar and N. Kamsah, "Enhancement of thermal comfort in a large space building," *Alexandria Engineering Journal*, vol. 58, no. 1, pp. 49 – 65, 2019.
- [4] I. 7730, "Ergonomics of the thermal environment—analytical determination and interpretation of thermal comfort using calculation of the pmv and ppd indices and local thermal comfort criteria, third ed. international standards organization, geneva, ref no. iso 7730:2005(e)."
- [5] M. Bojic and F. Yik, "Locating air-conditioners and furniture inside residential flats to obtain good thermal comfort," *Energy and Buildings*, vol. 34, no. 7, pp. 745 – 751, 2002.
- [6] A. Stamou and I. Katsiris, "Verification of a cfd model for indoor airflow and heat transfer," *Building and Environment*, vol. 41, no. 9, pp. 1171 – 1181, 2006.
- [7] L. G. Aragão, "Avaliação da Eficiência Energética do Sistema de Condicionamento de Ar do Museu do Universo - Planetário da Gávea," 2014.
- [8] A. P. de Castro, "Análise da Circulação do Ar e do Comportamento Higrotérmico do Museu do Universo - Planetário da Gávea," 2016.



SEMI-LAGRANGEAN METHOD APPLIED IN THE CONJUGATED HEAT PROBLEM USING AN AXISYMMETRICAL STREAM FUNCTION-VORTICITY FORMULATION

Author: Luís Henrique Carnevale da Cunha¹ lh.carnevale@gmail.com
Advisors: ¹; Gustavo R. Anjos²
¹ Rio de Janeiro State University
² Rio de Janeiro Federal University

PPG-EM Seminars: season 2019
<http://www.ppgem.uerj.br>

December 12, 2019

Keywords: Conjugated Heat Transfer, Stream Function-Vorticity, Semi-Lagrangian Method

1 Introduction

This paper shows the use of the Finite Elements Method (FEM) for a conjugated heat problem in axisymmetrical coordinates. Conjugated heat problems have numerous applications, such as the cooling of electronic components with refrigerant fluid through microchannels between the components (seen in [5]). Being able to predict the behavior of heat transport between a solid and a fluid medium is the main goal for this type of problem.

The stream function-vorticity formulation was chosen to simulate the fluid flow because of the uncoupling of the velocity and pressure from the Navier-Stokes equations, permitting the use of linear triangular elements. In this formulation the flow is represented by the stream function ψ and the vorticity ω , the velocity is then calculated from the stream function. An example of the FEM used with this formulation is presented in [4] and with conjugated heat in [2].

In this work we propose the use of the Semi-Lagrangian Method (SL), as in [1], for discretizing the material derivatives and increase the numerical stability of the simulations. And also the use of a FEM formulation to calculate the vorticity boundary condition which is more commonly obtained by finite-difference schemes (see [6]).

2 Methodology

2.1 Governing Equations

The governing equations for the stream function-vorticity formulation in cylindrical coordinates for an axisymmetric flow, as found in [3], are:

$$\frac{D\omega}{Dt} = \frac{\omega v_r}{r} + \nu \left[\frac{\partial}{\partial r} \left(\frac{1}{r} \frac{\partial r \omega}{\partial r} \right) + \frac{\partial^2 \omega}{\partial z^2} \right] \quad (1)$$

$$\omega = \frac{\partial v_r}{\partial z} - \frac{\partial v_z}{\partial r} \quad (2)$$

$$\frac{\partial}{\partial r} \left(\frac{1}{r} \frac{\partial \psi}{\partial r} \right) + \frac{\partial^2}{\partial z^2} \left(\frac{\psi}{r} \right) = -\omega \quad (3)$$

$$(v_z, v_r) = \left(\frac{1}{r} \frac{\partial \psi}{\partial r}, -\frac{1}{r} \frac{\partial \psi}{\partial z} \right) \quad (4)$$

where r is the radius, z is the coordinate along the symmetry axis, t is the time variable, ν is the kinematic viscosity, ω_θ is the vorticity component in the θ direction, v_r de radial velocity and v_z being the axial component. The axisymmetric temperature equation for a medium with thermal diffusivity α is:

$$\frac{DT}{Dt} = \alpha \left[\frac{1}{r} \frac{\partial}{\partial r} \left(r \frac{\partial T}{\partial r} \right) + \frac{\partial^2 T}{\partial z^2} \right] \quad (5)$$

2.2 Semi-Lagrangian Method

The SL method is used to improve overall numerical stability therefore making it possible to use larger time steps in the simulations. Having a stable method is of utmost importance for flows with high Reynolds number. The method consists in discretizing the material derivative for a function scalar f as:

$$\frac{Df}{Dt} = \frac{f_i^{n+1} - f_d^n}{\Delta t} \quad (6)$$

where f_d^n is the function at the time n in the called departure position, f_i^{n+1} is the function at the time $n+1$ in the current position. The departure position is $x_d = x_i - \mathbf{v} \Delta t$, x_i being the position of the nodal points in the mesh. The function f_d^n is calculated by interpolation from f_i^n .

2.3 Matricial Equatins

The final set of equations discretized in space by the Galerkin FEM and discretized in time with the SL is:

$$\left(\nu \mathbf{K} + \nu \mathbf{M}_3 - v_r \mathbf{M} + \frac{\mathbf{M}}{\Delta t} \right) \omega_i^{n+1} = \frac{\mathbf{M}}{\Delta t} \omega_d^n \quad (7)$$

$$(\mathbf{K} + 2\mathbf{G}_r) \psi_i^{n+1} = \mathbf{M}_2 \omega_i^{n+1} \quad (8)$$

$$\left(\frac{\mathbf{M}}{\Delta t} + \alpha \mathbf{K}\right) \mathbf{T}_i^{n+1} = \frac{\mathbf{M}}{\Delta t} \mathbf{T}_d^n \quad (9)$$

where \mathbf{M} , \mathbf{K} , \mathbf{G} are the FEM mass, stiffness and gradient matrices respectively.

3 Results

The conjugated heat problem shown in Fig. 1 represents a hollow cylinder with a thick wall (solid region) and internal temperature T_{wall} being cooled by the flow in an annular tube enclosing it. The fluid has temperature T_{in} on $z = 0$. Both left and right sides of the cylinder and the outside wall of the flow section are considered thermally isolated. In this problem it is possible to compare the flow simulation to an analytic result given by the Hagen-Poiseuille flow in an annular section.

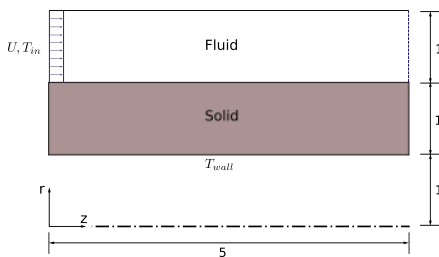


Figure 1: Proposed conjugate heat problem.

Viscosity	$\mu = 1$
Fluid density	$\rho = 1000$
Fluid thermal diffusivity	$\alpha_f = 0.001$
Solid thermal diffusivity	$\alpha_s = 0.05$
Δt	0.05
Number of nodes	2328
Number of elements	4779

Table 1: Parameters used for the numerical simulation. The parameters used in the simulation were arbitrarily defined and are found in Tab. 1. The boundary conditions were: $T_{wall} = 10$; $T_{in} = 1$; $U = 2$; $\psi = 0$ on inner wall and $\psi = 3.34$ on outer wall. In Fig. 2 (a), (b) and (c), the numerical results for the Hagen-Poiseuille flow were compared to the analytical solution and there is a little difference in the velocity, stream-function and vorticity profiles but overall they show a similar behavior. The complete numerical solution of the temperature presented in Fig. 3.

4 Conclusions

For this paper, both FEM and SL were validated with the Hagen-Poiseuille flow in an annular tube and a simulation of a conjugated heat transfer problem using the proposed method was presented. A further step in the work is the use of the Arbitrary Lagrangian-Eulerian (ALE) formulation, already implemented and being tested.

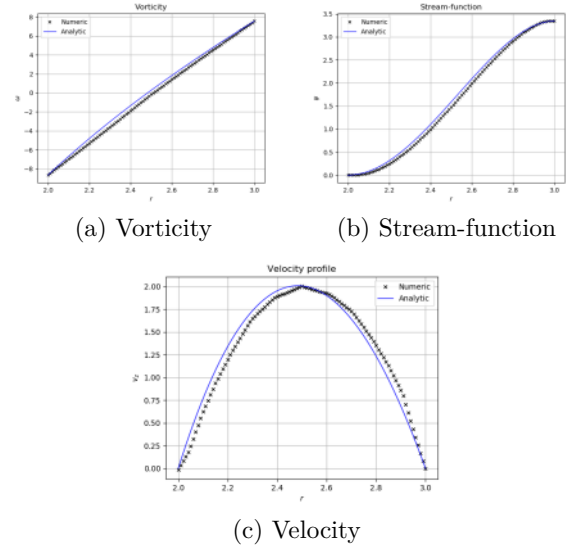


Figure 2: Comparison between numerical and analytical solution of the annular flow on $z = 5$.

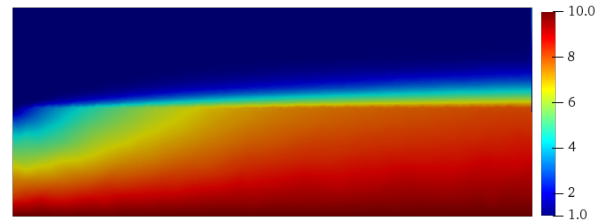


Figure 3: Simulation of the temperature distribution.

References

- [1] Gustavo Rabello Anjos. *A 3D ALE Finite Element Method for Two-Phase Flows with Phase Change*. PhD thesis, École Polytechnique Fédérale De Lausanne, 2012.
- [2] G. Cesini, M. Paroncini, G. Cortella, and M. Manzan. Natural convection from a horizontal cylinder in a rectangular cavity. *International Journal of Heat and Mass Transfer*, 1998.
- [3] R.L. Panton. *Incompressible Flow*. Developmental clinical psychology and psychiatry. Wiley, 1996.
- [4] M. F. Peeters, W. G. Habashit, and E. G. Dueck. Finite element stream function-vorticity solutions of the incompressible navier-stokes equations. *International Journal for Numerical Methods in Fluids*, 1987.
- [5] Sylwia Szczukiewicz. *Thermal and Visual Operational Characteristics of Multi-Microchannel Evaporators using Refrigerants*. PhD thesis, École Polytechnique Fédérale De Lausanne, 2012.
- [6] M. Vynnycky, S. Kimura, K. Kanev, and I. Pop. Forced convection heat transfer from a flat plate: the conjugate problem. *International Journal of Heat and Mass Transfer*, 1998.



UNCERTAINTIES QUANTIFICATION ON CREEP REMAINING LIFE PREDICTION MODELS

Author: Victor Maudonet¹ victor.maudonet@uerj.br
Advisors: Americo Cunha Jr¹ ; Carlos Frederico Trotta Matt²

¹ Rio de Janeiro State University

² Cepel

PPG-EM Seminars: season 2019

<http://www.ppgem.uerj.br>

December 20, 2019

Keywords: Creep, uncertainty quantification, global sensitivity analysis, maximum entropy principle

1 Introduction

With the increase in national energy demand [1], the interest in techniques and models that allow to reliably predict and evaluate the remaining creep life of industrial equipment, especially those operating at high temperatures, ensuring integrity, has increased. This need is justified by reduced costs, increased safety and extended service life, as these materials often remain in operation even with their design lives already exceeded. Moreover, in the early stages of design, creep life prediction is still one of the biggest challenge related to the reliability of high temperature engineering materials [2]. Creep damage is a phenomenon influenced macroscopically by temperature and stress and is cumulative, i.e. when there is more than one creep mechanism acting on a material its effects are added, accelerating the degradation of the material [3]. The good creep resistance properties of 1Cr-Mo-V steels make them widely used in high temperature equipment [4]. These properties are due to the presence of chromium and molybdenum, which promote solid solution hardening and carbide precipitation, and some of these act directly on the creep mechanisms, such as the movement of dislocations, which tend to be anchored or delayed. In their course when they come across the carbides [5]. Although several creep life prediction models have been proposed in the last decades, the vast majority of them doesn't account for the dispersion of experimental creep life data. Even with the strong evidence that creep life prediction is a stochastic process, corroborated by several experiments performed in different laboratories around the world, the creep life prediction models traditionally used are all deterministic. There is no variability associated with its parameters. Therefore, more research is needed to develop sufficiently general models that take into account the dispersion of experimental data for reliable creep life prediction of materials operating at high temperatures.

2 Objectives

The present work aims to propose a probabilistic version for some creep life prediction models to quantify the uncertainty associated with the parameters of these models. This will be done from a parametric probabilistic approach considering few experimental data, which is typical of noble steels like 1Cr-Mo-V steel. Based on statistical information extracted from available experimental data, a theoretical uncertainty quantification framework based on the maximum entropy principle and Monte Carlo simulations was developed to determine the probability distribution of the input parameters of the Larson-Miller model.

3 Methodology

3.1 Deterministic modeling

The creep life prediction model developed by Larson and Miller is the most widely used in engineering projects. This model is actually a parametric method of data extrapolation, as it is absolutely impossible to simulate the field operating conditions in the laboratory. In this sense, accelerated creep tests are performed under more severe operating conditions and data extrapolation may be used to make predictions. In addition, parametric methods for extrapolating experimental creep data consist of grouping the input parameters stress, temperature, and time to rupture. The Larson-Miller parameter is obtained by the following equation:

$$PLM = T(C + \log t_r) \quad (1)$$

where, P is the Larson-Miller parameter, which is a stress function $f(\sigma)$; T is the absolute temperature which the component is subjected; C is the dimensionless constant that depends on the material under analysis and t_r is the time to rupture, usually expressed in hours. Then, knowing the operating condition to which the material is being subjected, it is possible to determine the Larson-Miller parameter and the time to rupture is calculated deterministically by the following equation:

$$t_r = 10^{\frac{PLM}{T} - C} \quad (2)$$

3.2 Probabilistic modeling

It is worthwhile to present an overview of a conventional deterministic approach compared with the proposed probabilistic approach. Figure 2 depicts an overall comparison between the two approaches. In conventional deterministic approaches, deterministic quantities for each Larson-Miller model input parameters are defined and the model equations, Eqs. (1) and (2), are solved deterministically in order to obtain the output parameters. For the proposed probabilistic approach, first, probability distributions of the input random variables need to be defined using uncertainty modeling techniques. Then the uncertainties of the input parameters need to be propagated through the model equations and finally, statistical inference is used to obtain the probability distributions of the Larson-Miller model output parameters.

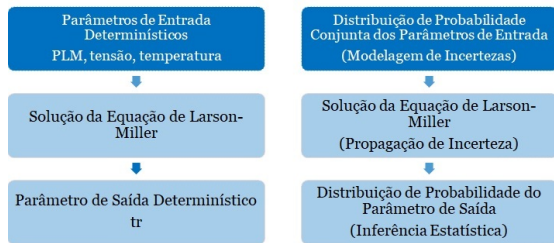


Figure 1: Comparison between deterministic and probabilistic approaches

3.3 Global sensitivity analysis

In order to describe how the variability of the model response t_r is affected by the variability of each input parameter ($T, \sigma, C, a_0, a_1, a_2$) and the combination of these parameters, a global sensitivity analysis was performed. The parameters a_0, a_1, a_2 are the coefficients of the polynomial fit for the relationship between the Larson-Miller parameter and the stress. This analysis is also useful for identifying unimportant parameters, thereby reducing the model. To perform such analysis, the Sobol sensitivity indices were selected. The Sobol indices for the input parameters of the Larson-Miller model were calculated from two different methodologies, via Monte Carlo method and via Polynomial Chaos Expansion. At this stage of the research this is the only analysis that was performed.

4 Results and discussion

The first order Sobol indices calculated by both methods are presented in Figure 2. The blue represents the Polynomial Chaos Expansion and green represents the Monte Carlo method. These indices represent the effect of each parameter separately. The total indices (the sum of the contribution of the interaction of the parameters) are presented in Figure 3.

Analyzing the obtained results, it can be verified that the first order effects of the parameters are relatively low, that is, the influence of each isolated parameter is low. In contrast, the second, third and fourth order effects are more relevant, this shows that the interaction be-

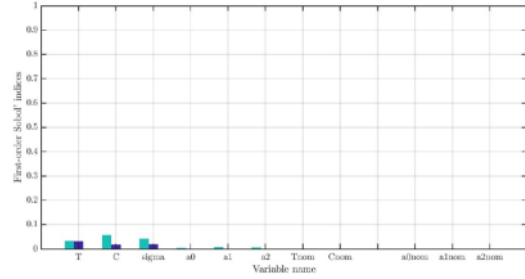


Figure 2: First order Sobol indices calculated by the Monte Carlo Method and the Polynomial Chaos Expansion.

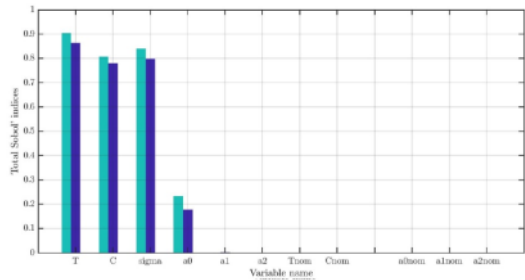


Figure 3: Total Sobol indices calculated by the Monte Carlo Method and the Polynomial Chaos Expansion.

tween the input parameters is significant. Furthermore, according to this analysis, the model can be reduced, the Sobol indices of the parameters a_1 and a_2 presented negligible values, so these parameters are negligible and are not taken into consideration in subsequent analyzes.

5 Conclusions

- The isolated effect of the input parameters of the Larson-Miller model on the time to rupture is low;
- The interaction effect of the input parameters of the Larson-Miller model is significant;
- The values of the sobol indices for parameters a_1 and a_2 were negligible and these parameters were disregarded;
- The Larson-Miller model can be reduced.

6 References

- [1] Empresa de Pesquisa Energética – EPE. Previsão de Demanda de Energia Elétrica. Rio de Janeiro, 2017.
- [2] AMERICAN SOCIETY FOR METALS - ASM, Fatigue and Fracture, Metals Handbook, vol 19, Ohio, 1996.
- [3] SHACKELFORD, J.F., Ciência dos Materiais, Pearson, 6^a ed., 2008.
- [4] HOLDSWORTH, S.R., Creep Resistant Materials for Steam Turbines, Encyclopedia of Materials: Science and Technology, 2001, pp 1836-1839.
- [5] DIETER, G.E., Metalurgia Mecânica, Guanabara Dois, 2^a ed, Rio de Janeiro, 1981.



EVALUATION OF THERMAL AND EVAPORATIVE EFFICIENCY OF SPRAY-DRYER

Author: Alexandre Vasconcelos Rodrigues¹ avrodrigues.rj@gmail.com

Advisor(s): Prof. PhD Manoel Antônio Fonseca da Costa Filho¹

¹ Rio de Janeiro State University

PPG-EM Seminars: season 2019
<http://www.ppgem.uerj.br>

Dec. 03, 2019

Keywords: Spray Drying, Energy efficiency, Drying technology

1 Introduction

Spray-drying is one of the most important continuous dryers in the industry, despite high installation and operating costs. Its application is justified because of its ability to convert solutions, suspensions or pastes into high quality and homogeneous dry powder. Drying is one of the most energy-intensive industrial processes [3] and to maintain its sustainability, the operation must be effective due to a rising energy cost and growing concerns over greenhouse gas emissions. A experimental evaluation of energy efficiency was carried out on a industrial process of a pharmaceutical product using spray drying with direct gas-fired heating operating with liquefied petroleum gas - LPG. In these process a concentrated wet slurry is injected by a rotary disk atomizer co-currently with gases at 190 °C. Dry powder-like is recovered from exhaust stream by cyclone.

2 Methodology

A detailed analysis of spray drying presents as a complex task. The complicated flow pattern and particle dynamics need a sophisticated approach with a computational fluid dynamic tool. This work evaluated the dryer thermal and evaporative efficiency based on overall heat and mass balances to identify opportunities for minimization of energy consumption. Figure 1 shows a simplified diagram of process with parameters variables and inspection points indicated. recovery product cyclones is omitted for simplifications reason. Atomizing, wall sweep and drying air are considered only one flux to the dry chamber: \dot{m}_{aci} . When hydrocarbon are burned in air, water is produced. the complete combustion of 1kmol of standard LPG, reduced equation: $C_{3,71}H_{8,50}$, produces $4,23\text{kmol}$ of water and contributes to the moisture content in the drier air. Applying first law of thermodynamic on these control volumes, but neglecting kinetic and potential energy and assuming that there will be no energy consumption by product crystallization nor no chemical reaction in the chamber, the energy balance in steady-state can

be stated as

$$(\dot{m}_{ao}h_{ao} + \dot{m}_p)_{out} - (\dot{m}_{ai}h_{ai} + \dot{m}_{LPG} \cdot LHV + \dot{m}_s h_s)_{in} - Q_l = 0 \quad (1)$$

where \dot{m}_{ao} , \dot{m}_p are inlet and outlet air mass flow rate, \dot{m}_s is inlet slurry, \dot{m}_p outlet recovery product form stream, \dot{m}_{LPG} and LHV mass flow rate and its lower heating value. Q_l represents heat loss from shell. Specific enthalpy of slurry feed and finished product referenced to $T_{ref} = 273\text{K}$ are given by [2]

$$h_s = (Cp_s + x_{sl}Cp_l)T_s \quad e \quad h_p = (Cp_s + x_{pl}Cp_l)T_p \quad (2)$$

humid air enthalpy can be calculated as [1]

$$h_{ai} = 1,006t + \omega(2501 + 1,86t) \quad (3)$$

The process parameters necessary to perform de analysis was collect from indicated points in diagram (1)

- Points 1 and 5: inlet air humidity measured with semiconductor sensor and temperature with type K thermocouple;
- Point 2 LPG gas flow rate with turbine meter;
- Points 7: gases flow rate with Type S Pitot tube and temperature, type K thermocouple;
- Points 3: mass flow rate and humidity of wet slurry feed. Data collected form plant process instruments.
- Point 4: mass flow rate and humidity content of finished product form;
- Point 5: inlet air to pneumatic transportation system.

Dryer chamber absolute humidity can be calculated as

$$\omega_{aci} = \frac{(\omega_{ai}\dot{m}_{ai} + c\dot{m}_{LPG})}{\dot{m}_{aci}} \quad (4)$$

where c in the amount of water produced per mass of fuel. Outlet moisture of point 6 was estimated by inlet air humidity, combustion water generation and water extracted from wet feed. Due aseptic reasons the air mass flow rate prior to chamber outlet let was not allowed to be measured, then air flow of pneumatic

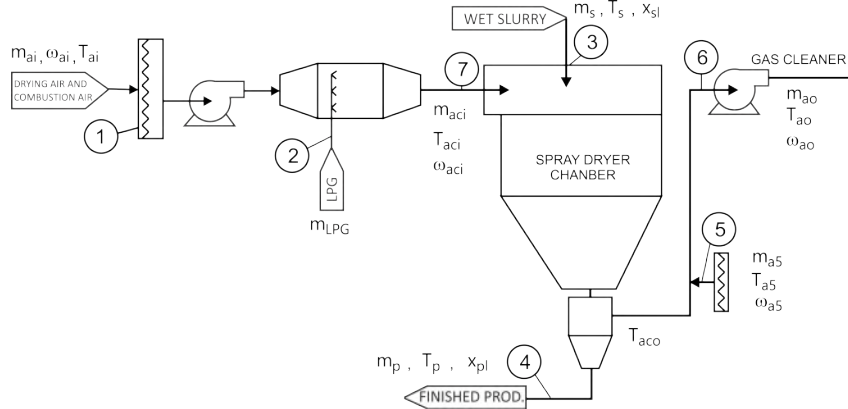


Figure 1: Simplified process diagram of the spray drying system

transportation m_{a5} should be considered. Hypotheses that no water is removed during pneumatic transportation nor at product recover from hot gas steam in the cyclones. Another hypotheses, there is no vapor leaking in dry chamber. Calculated and measured data are shown on table 1 energy required in the dryer can

Table 1: Relevante Spray dryer parameters

parameter	value	parameter	value
ponto 1		ponto 2	
m_{ai}	12.837 kg/h	m_{LPG}	43,66 kg/h
ω_{ai}	0,0142 kg w/kg air	LHV	46.000 kJ/kg
T_{ai}	35,10 °C	ponto 3	
h_{ai}	71,65 kJ/kg	$m_s(wet)$	690 kg/h
ponto 7		x_{sl}	185,72 % db
m_{aci}	12.880 kg/h	T_s	30,00 °C
ω_{aci}	0,0191 kg w/kg air	h_s	303,62 kJ/kg
T_{aci}	190,00 °C	ponto 4	
h_{aci}	245,61 kJ/h	$m_p(dry)$	241,3 kg/h
ponto 6		x_{pl}	3,62 % db
m_{ao}	18.803 kg/h	T_p	96,00 °C
ω_{ao}	0,0365	h_p	729,26 kJ/kg
T_{ao}	70,50 °C		
h_{ao}	167,00 kJ/kg	$\dot{m}_w \text{ evap}$	440,50 kg/h

be expressed in eq. (5), where h_w is latent heat of vaporization

$$E_{ev} = m_p(x_{sl} - x_{pl})h_w \quad (5)$$

The spray drier performance may be evaluated in two ways: thermal and evaporative efficiency. First η_t relates the ratio of energy used for moisture evaporation E_{ev} at the slurry feed temperature to total energy supplied to the dryer E_t [4]

$$\eta_t = \frac{E_{ev}}{E_t} \cdot 100\% \quad \therefore \quad \eta_t = 30,93\% \quad (6)$$

For low humidity and low temperature when the specific heat capacities may be considered constant, Mujundar (2015) [5] proposed a simplified equation for thermal efficiency. Kudra (2012) [4] pointed problems with this approach that may leading to a unreal value because do not consider losses. Its clear on (7) the problem. Almost 100 % error

$$\eta_{ts} = \frac{T_{aic} - T_{aoc}}{T_{aic} - T_{amb}} \cdot 100\% \quad \therefore \quad \eta_{ts} = 60,70\% \quad (7)$$

Thermal efficiency only indicate part of dryer performance [4], Evaporative efficiency compare the dryer

with the maximum efficiency possible η_{ev} which is attained when the outlet air temperature reach the adiabatic saturation temperature T_{sat}

$$\eta_{ev} = \frac{T_{aci} - T_{aco}}{T_{aci} - T_{sat}(\omega_{aco})} \quad \therefore \quad \eta_{ev} = 14,91\% \quad (8)$$

3 Results and discussion

Drying efficiency is directly related with temperature difference between inlet and outlet temperature then as much higher the difference is better, but inlet temperature is limited by resistance of product to thermal degradation[6], and outlet, by the maximum humidity content allowed with equilibrium humidity [2]. If product permits, mechanically reduction of slurry humidity is always cheaper then evaporation. Heat recovery form exhaust gases to preheat the inlet air, using flat heat exchange increase thermal efficiency and flue gas recirculation increase de evaporative efficiency. Its important that all equipment need be designed for CIP (Cleaning in process procedure).

References

- [1] ASHRAE. *Fundamentals*. American Society of Heating, refrigeration and air-Conditioning Engineers, 2017.
- [2] B. Golman and W. Julklang. Simulation of exhaust gas heat recovery from a spray dryer. *Applied thermal engineering*, pages 08 –45, 2014.
- [3] T. Kudra. Energy aspects in drying. *Drying Technology: An International Journal*, 22:191 –932, 2007.
- [4] T. Kudra. Energy performance of convective dryers. *Drying Technology: An International Journal*, 30:1190 –1198, 2012.
- [5] Arun S. Mujundar, editor. *Handbook of Industrial Drying*. CRC Press, 4 edition, 2015.
- [6] J.T. Toneli, L. B. Monteiro, M. Aurelio J. Briso, and D. Moraes. Effect of the outlet air reuse on thermal efficiency of a pilot plant spray dryer with rotary atomizer. *Chemical Engineering Transactions*, 32, 2013.



A DATA-DRIVEN APPROACH FOR INFERENCE OF THE EVOLUTION EQUATION OF A DUFFING OSCILLATOR

Author: Diego Matos Silva Lopes¹ diego.matos@uerj.br
Advisor(s): Americo Barbosa da Cunha Junior¹

¹ Rio de Janeiro State University

PPG-EM Seminars: season 2019
<http://www.ppgem.uerj.br>

Dez 19, 2019

Keywords: Duffing oscillator, machine learning, data-driven inference, sequential threshold least-squares.

1 Abstract

As more and more data is available on a daily basis, it is natural to seek to infer relevant information embedded in these datasets. In the context of dynamical systems, this idea translates into the use of observations (data) to infer the evolution law. In this sense, machine learning techniques are getting more space in the analysis and synthesis of dynamical systems. This paper uses regularized data-driven regression algorithm to infer the evolution law of a Duffing oscillator, using a library of mathematical functions obtained from a dataset generated from the underlying physical system.

2 Introduction

A dataset obtained from the sampling of a dynamic system can be used to develop a library of testing functions from which one can perform an sequential threshold least-squares that allow to infer the system dynamic evolution law [1][2]. In this sense, this paper illustrates the basic principle behind the sequential threshold least-squares in the reconstruction of the evolution law of a Duffing oscillator.

3 Data-driven identification procedure

If a dynamical systems have a small amount of terms in its evolution law, its is very likely it can be parametrized by a sparse linear combination of elementary functions. In this sense, the key idea here is to construct, with aid of available observations (data) from the original system, a library of polynomial functions in a way that a sparse linear combination of them may be enough to approximate the evolution law.

For sake of identification of the coefficients (coordinates) of this functional representation a machine learning approach, based on a sequential threshold least-squares regression, is employed. In this method a threshold is defined so that the regression coefficients that have their absolute value below this parameter are considered zero, being the regression computed again without these terms.

Since the database is organized as follows:

$$\mathbf{X} = \begin{bmatrix} \mathbf{x}^T(\mathbf{t}_1) \\ \mathbf{x}^T(\mathbf{t}_2) \\ \vdots \\ \mathbf{x}^T(\mathbf{t}_m) \end{bmatrix} = \begin{bmatrix} x_1(t_1) & x_2(t_1) & \dots & x_n(t_1) \\ x_1(t_2) & x_2(t_2) & \dots & x_n(t_2) \\ \vdots & \vdots & \ddots & \vdots \\ x_1(t_m) & x_2(t_m) & \dots & x_n(t_m) \end{bmatrix} \quad (1)$$

$$\dot{\mathbf{X}} = \begin{bmatrix} \dot{\mathbf{x}}^T(\mathbf{t}_1) \\ \dot{\mathbf{x}}^T(\mathbf{t}_2) \\ \vdots \\ \dot{\mathbf{x}}^T(\mathbf{t}_m) \end{bmatrix} = \begin{bmatrix} \dot{x}_1(t_1) & \dot{x}_2(t_1) & \dots & \dot{x}_n(t_1) \\ \dot{x}_1(t_2) & \dot{x}_2(t_2) & \dots & \dot{x}_n(t_2) \\ \vdots & \vdots & \ddots & \vdots \\ \dot{x}_1(t_m) & \dot{x}_2(t_m) & \dots & \dot{x}_n(t_m) \end{bmatrix} \quad (2)$$

Considering the library of elementary functions defined by the matrix

$$\Theta(\mathbf{X}) = [\mathbf{1} \quad \mathbf{X} \quad \mathbf{X}^{\mathbf{P}_2} \quad \dots \quad \mathbf{X}^{\mathbf{P}_n}], \quad (3)$$

where $\mathbf{X}^{\mathbf{P}_n}$ represents all dimension combinations that form a n -degree polynomial, the evolution law for the dynamical system state \mathbf{X} is obtained from

$$\dot{\mathbf{X}} = \Theta(\mathbf{X})\Xi + \eta\mathbf{Z}, \quad (4)$$

where Ξ determines which functions are activated and their weights, \mathbf{Z} is a matrix with zero-mean normally distributed random values, and η is the corresponding standard deviation.

4 Numerical experiment

For sake of illustration of the machine learning identification procedure, a Duffing like damped dynamical system is considered

$$\dot{x}_1 = x_2, \quad \dot{x}_2 = -0.1x_2 + x_1 - x_1^3. \quad (5)$$

A comparison between the “exact” (reference) response of this dynamic system and data-driven time series and phase space trajectory, inferred by the identification procedure, can be seen in Figures 1 and 2.

The “exact” and data-driven identified dynamics with initial conditions $x_1(0) = 2$ and $x_2(0) = 0$. The “exact” solution is obtained by RK45 method with 6000

equally spaced time-steps between 0 and 60 seconds. The dataset has 1200 points randomly taken from the reference time series. The data-driven solution is obtained from a mathematical functions library with polynomials functions up to fifth degree, standard deviation 0.1 and threshold value 0.075.

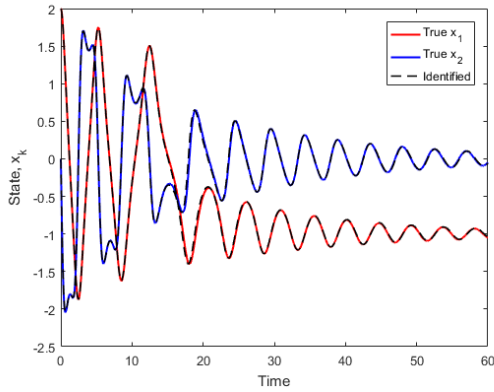


Figure 1: “Exact” and data-driven time series for x_1 and x_2 .

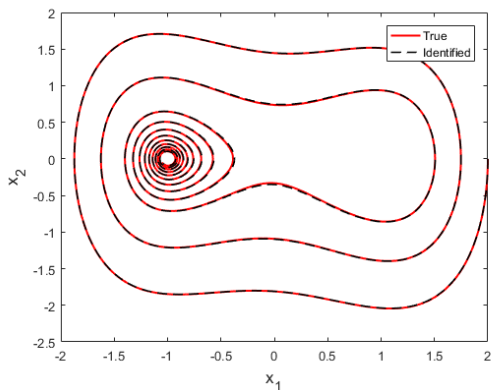


Figure 2: “Exact” and data-driven phase space trajectory.

5 Conclusions

The machine learning approach employed is able to recognize with incredible precision the law of evolution of the Duffing oscillator, even with high intensity of noise polluting the database, demonstrating to be an effective method for inferring the evolution law of dynamic systems.

6 Acknowledgements

The authors are indebted to the Brazilian agencies CNPq, CAPES, and FAPERJ for the financial support given to this research.

References

- [1] S. L. Brunton, J. L. Proctor, and J. N. Kutz. Discovering governing equations from data by sparse identification of nonlinear dynamical systems. *Proc-*

ceedings of the National Academy of Sciences of the United States of America, 113:3932–3937, 2016.

- [2] Y. Yuan, J. Li, L. Li, F. Jiang, X. Tang, F. Zhang, S. Liu, J. Goncalves, H. U. Voss, X. Li, J. Kurths, and H. Ding. Machine discovery of partial differential equations from spatiotemporal data. 2019.



EMPLOYING 0-1 TEST FOR CHAOS TO CHARACTERIZE THE CHAOTIC DYNAMICS OF A GENERALIZED GAUSS ITERATED MAP

Author: Marcos Vinicius Issa¹ marcos.issa@uerj.br
Advisor(s): Americo Cunha Jr¹

¹ Rio de Janeiro State University

PPG-EM Seminars: season 2019
<http://www.ppgem.uerj.br>

Dec 3, 2019

Keywords: Nonlinear dynamics, Chaotic system, Generalized Gauss iterated map, 0-1 Test for chaos.

1 Introduction

Nonlinear systems are constantly studied in the scientific literature as attempts to reproduce complex phenomena with greater reliability. Several of these systems are highly dependent on the parameters and/or initial conditions and may exhibit chaotic behavior for some configurations. Since chaotic behavior may or may not be useful in applications of interest, it is crucial to identify under what conditions such behavior can manifest in a dynamical system [2].

When dealing with a system for which the dynamics is unknown, the exponents of Lyapunov [2] are often used for classification of the dynamic regime of operation in regular or chaotic. However, the computational cost associated with this method is very high, due to the required eigenvalue calculations. So, when in possession of a large system or costly computing system, the proposed 0-1 test for chaos by Gottwald and Melbourne [3] shows up a good balance between theoretical certification and fast processing.

2 Gauss iterated map

2.1 Map description

The standard Gauss iterated map uses a zero-mean unit-amplitude Gaussian as evolution law, having only two parameters: (i) the width α , interpreted as the variance inverse in a probabilistic contexts; and (ii) the offset β [4]. Therefore, the map evolution law is written as

$$x_{n+1} = \exp(-\alpha x_n^2) + \beta. \quad (1)$$

Here this map generalized by adding two other parameters, the scale γ , and the mean δ . Supplementing this map with an initial condition $x_0 = a$, the evolution law of this new generalized Gauss map is described by the following (discrete) initial value problem

$$\begin{cases} x_{n+1} = \gamma \exp(-\alpha(x_n - \delta)^2) + \beta, \\ x_0 = a. \end{cases} \quad (2)$$

2.2 Presence of chaos and regularity

Figure 1 shows a bifurcation diagram of the dynamical system described (2), where it can be observed a qualitative variation of the response as γ assumes 3001 values in the range $-10 \leq \gamma \leq 10$, with $\alpha = 4.9$, $\beta = 0.5$, $\delta = 0$, $x_0 = 0.2$, for a temporal evolution of the map with 5000 steps. In this figure, three scenarios can be highlighted: (i) regular dynamics of period 1 at $\gamma = 1$; (ii) regular dynamics of period 10 at $\gamma = -2.9$; (iii) a chaotic dynamics at $\gamma = -1.05$. Also remember that, with $\delta = 0$ and $\gamma = 1$, the response is equivalent to that of the standard Gauss map.

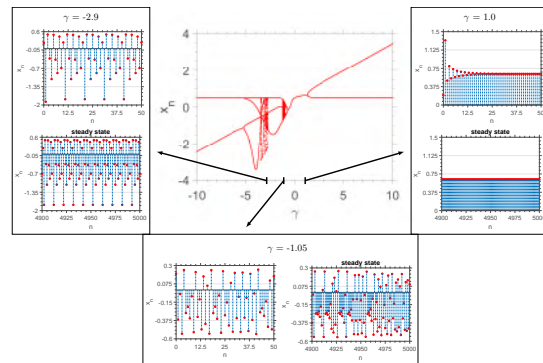


Figure 1: Bifurcation diagram of the generalized Gauss iterated map with $\alpha = 4.9$, $\beta = 0.5$, $\delta = 0$, $x_0 = 0.2$ and $-10 \leq \gamma \leq 10$.

3 The 0-1 test for chaos

The 0-1 test is the binary test for chaos identification that applies a change of coordinates from physical coordinates $(\phi(t), \dot{\phi}(t))$ to a pair of extended coordinates (p_c, q_c) , parameterized by an angle c (see [1] for details). From this new coordinates, a time-averaged mean square displacement M_c is extracted, and the classifier K_c can be calculated. The test is repeated for several values of c , and $K = \text{median}\{K_c\}$ is employed as the classifier for the dynamic regime of the time-series $\phi(t)$. It can be demonstrated that, theoretically that $K_c \in \{0, 1\}$, so that, numerically $K \approx 0$ for regular dynamics, and $K \approx 1$ in the chaotic case [3]. The Figure 2 shows a schematic representation of the test.

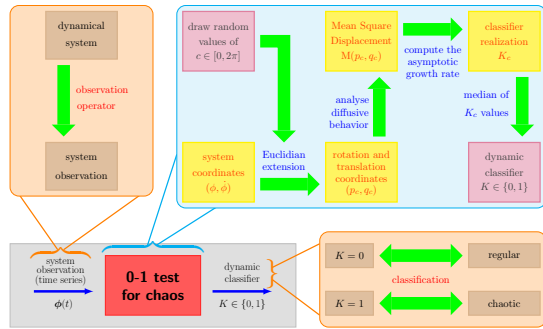


Figure 2: Schematic representation of the 0-1 test for chaos where is detailed the method’s steps such as well as the classification and obtaining of a system observable.

4 Numerical experiments

4.1 Validation of 0-1 test classifier

Some results are shown in Figures 3 and 4, where one can see the extended dynamics in (p, q) coordinates, the evolution of the square distance MSD , and the classifier samples K_c as function of the values of c . In Figure 3 one can see that, for $\alpha = 4.9, \beta = 0.5, \gamma = -1.05$ and $\delta = 0$, the system behavior is chaotic, since the extended dynamics in (p, q) coordinates is diffusive [1, 3]. Note from Figures 3b and 3c that 0-1 test for chaos correctly detect chaotic behavior. On other hand, regularity can be observed in Figure 4, once the extended dynamics is limited [1, 3].

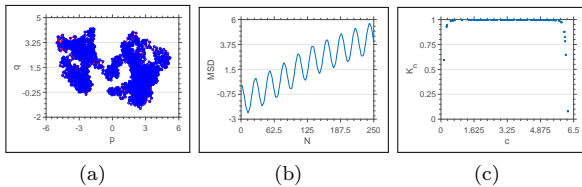


Figure 3: Test 0-1 for chaos with $\alpha = 4.9, \beta = 0.5, \gamma = -1.05$ and $\delta = 0$. (a) extended dynamics in (p, q) coordinates, (b) the evolution of the square distance MSD , and (c) the classifier samples K_c as function of the values of c .

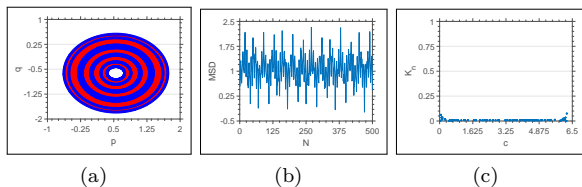


Figure 4: Test 0-1 for chaos with $\alpha = 4.9, \beta = 0.5, \gamma = 1$ and $\delta = 0$. (a) extended dynamics in (p, q) coordinates, (b) the evolution of the square distance MSD , and (c) the classifier samples K_c as function of the values of c .

4.2 Contour maps

With the classification test properly calibrated, more extensive results about the dynamics of the generalized

Gauss map with respect to the values of γ and δ can be extracted. A broad analysis is indicated by the contour maps in Figure 5. The regular behavior is indicated by the darkest blue points and chaos by the red ones. The parameters used are $\alpha = 4.9, \beta = 0.5, \gamma \in [-5, 5], \delta \in [-1, 1], x_0 = 0.2$, with 5000 iterations, $N_c = 300$, and a resolution of 100×100 points in (γ, δ) space. The result reveals two regions where chaos is more present: $(\gamma, \delta) \in [-3, 1] \times [-1, 0]$ and $(\gamma, \delta) \in [4, 5] \times [0, 0.5]$.

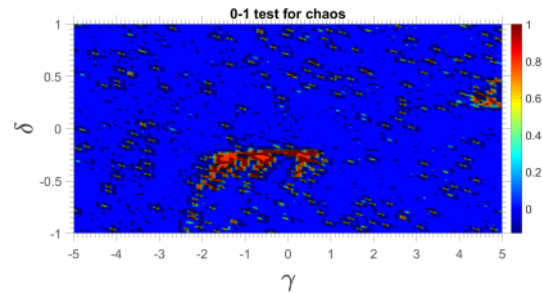


Figure 5: Contour map for $-5 \leq \gamma \leq 5, -5 \leq \delta \leq 5$, with $\alpha = 4.9, \beta = 0.5$, and $x_0 = 0.2$.

5 Final remarks

The 0-1 test for chaos is explored to classify the system dynamics and used to generate contour maps that reveal chaotic regions in the parameters space. These results allowed conclude that two regions with a huge presence of chaos exist. In future works the authors intend to use the 0-1 test to generate basins of attraction with respect to the parameters in order to study the system sensitivity to small changes on their nominal values.

Acknowledgments

The author is indebted to the Brazilian agencies Carlos Chagas Filho Research Foundation of Rio de Janeiro State (FAPERJ) under grants E-26/010.002.178/2015 and E-26/010.000.805/2018 and Coordenação de Aperfeiçoamento de Pessoal de Nível Superior - Brasil (CAPES) - Finance Code 001. This work had the collaboration of Michel Tosin (michel.tosin@uerj.br), Diego Matos (diego.matos@uerj.br) and Alexandre Nascimento (*in memoriam*).

References

- [1] D. Bernardini and G. Litak. An overview of 0-1 test for chaos. *J Braz. Soc. Mech. Sci. Eng.*, 38: 1433–1450, 2016. doi: 10.1007/s40430-015-0453-y.
- [2] P. G. Drazin. *Nonlinear Systems*. Cambridge University Press, 1992.
- [3] G. A. Gottwald and I. Melbourne. A new test for chaos in deterministic systems. *Proc. R. Soc. Lond. A*, 204:603–611, 2004. doi: 10.1098/rspa.2003.1183.
- [4] H. K. Sarmah, M. C. Das, T. K. Baishya, and R. Paul. Characterising chaos in gaussian map. *Int. J. Adv. Sci. Tech. Res.*, 9:160–172, 2016.



THE PIECEWISE CONSTANT THERMAL CONDUCTIVITY AND THE KIRCHHOFF TRANSFORMATION

Author: Alane Miguelis Falcão Magalhães¹ alane.miguelis@gmail.com
Advisor(s): Rogério Martins Saldanha da Gama¹
¹ Rio de Janeiro State University

PPG-EM Seminars: season 2019
<http://www.ppgem.uerj.br>

Dec 10, 2019

Keywords: Heat conduction, Kirchhoff transformation, piecewise constant thermal conductivity.

1 Introduction

In heat conduction problems it is common to consider the thermal conductivity of a material as a constant, in order to simplify the mathematical description and to give easy numerical simulations. However, such an assumption may give rise to inaccurate results, especially when there are large heat fluxes. It is known that the thermal conductivity of any real material depends on the temperature. In this case, the heat conduction problem becomes a nonlinear partial differential equation, because the thermal conductivity is expressed as a function of temperature. The Kirchhoff transformation is a procedure that rewrites the original problem in terms of a new quantity, and this avoids the need of working with a nonlinear equation.

2 Mathematical formulation

The equation (1), known by Fourier's Law of heat conduction, relates the heat flow to the temperature gradient. In this equation we have also the thermal conductivity, an intrinsic property of any material that describe its ability to conduct heat.

$$q = -k \text{grad} T \quad (1)$$

Analysing the energy balance during heat conduction in a solid material and considering a steady-state flow, we have the heat equation:

$$\text{div} q + \dot{q} = 0, \quad (2)$$

in which \dot{q} means internal heat generation.

From (1) and (2), we have:

$$\text{div}(k \text{grad} T) + \dot{q} = 0 \quad (3)$$

3 Methodology

3.1 Piecewise constant thermal conductivity

At this point, it is a good idea to consider the thermal conductivity as a piecewise constant function of the

temperature, with each part as its absolute temperature.

$$k = \hat{k}(T) = \begin{cases} k_1, & \text{for } T \leq T_1 \\ k_i, & \text{for } T_i \geq T > T_{i-1}, \quad i = 2, 3, 4, \dots, N \\ k_N, & \text{for } T > T_{N-1} \end{cases} \quad (4)$$

3.2 The Kirchhoff transformation

As $k = \hat{k}(T)$ for any $T > 0$, we can define:

$$\omega = K[T] = \int_0^T \hat{k}(\xi) d\xi \quad (5)$$

We can write the nonlinear heat equation as a linear one:

$$\text{div}(\text{grad} \omega) + \dot{q} = 0 \quad (6)$$

Assuming (4), the Kirchhoff transformation is given by:

$$\omega = K[T] = \int_0^T \hat{k}(\xi) d\xi = \begin{cases} k_1 T, & \text{if } T \leq T_1 \\ k_2(T - T_1) + k_1 T_1, & \text{if } T_2 \geq T > T_1 \\ k_3(T - T_2) + k_2(T_2 - T_1) + k_1 T_1, & \text{if } T_3 \geq T > T_2 \\ \vdots \\ \vdots \\ k_N(T - T_{N-1}) + k_{N-1}(T_{N-1} - T_{N-2}) + \dots + \\ + k_2(T_2 - T_1) + k_1 T_1, & \text{if } T > T_{N-1} \end{cases} \quad (7)$$

$$\omega = K[T] = \frac{1}{2}((k_1 + k_N)T +$$

$$+ \sum_{i=2}^N (k_i + k_{i-1})(|T - T_{i-1}| - T_{i-1})), \quad (8)$$

with $T_N > T_{N-1} > \dots > T_2 > T_1 \geq 0$.

3.3 The inverse of Kirchhoff transformation

Defining the nonnegative constants $\omega_1, \omega_2, \dots, \omega_{N-1}$ as follows

$$\omega_1 = \sum_{j=1}^i k_j (T_j - T_{j-1}),$$

$$1 \leq i \leq N - 1, \text{ with } T_0 = 0, \quad (9)$$

the inverse of the Kirchhoff transformation is unique and explicitly given by:

$$T = K^{-1}[\omega] = \frac{1}{2} \left(\frac{1}{k_1} + \frac{1}{k_N} \right) \omega + \sum_{i=2}^N \left(\frac{1}{k_i} - \frac{1}{k_{i-1}} \right) (|\omega - \omega_{i-1}| - \omega_{i-1}) \quad (10)$$

4 Example

Let us consider the thermal conductivity of the silicon as a function of the absolute temperature. We would approximate the thermal conductivity by means of the equation:

$$k = \hat{k}(T) = \left(\frac{1220}{\sqrt{T}(\ln T)} \right)^2 \quad (11)$$

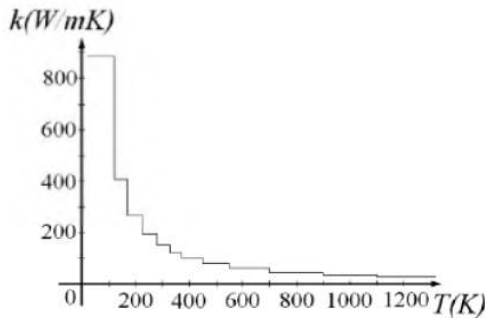


Figure 1: Thermal conductivity of the silicon. A piecewise constant approximation.

$$k_1 = \left(\frac{1220}{\sqrt{200}(\ln 200)} \right)^2; k_N = \left(\frac{1220}{\sqrt{1220}(\ln 1220)} \right)^2 \quad (12)$$

$$T_{APP} = \exp \left(\frac{1}{\frac{1}{\ln 200} + \frac{1}{(\ln 200)^2} - \frac{\omega_{APP}}{1200^2}} \right) \quad (13)$$

5 Results and conclusions

After the calculations above, we have the following results:

T	$\frac{\omega_{EX} - \omega_{APP}}{\omega_{EX}}$	T_{APP}	$\frac{ T - T_{APP} }{T}$
200.00	0.000%	200.00	0.000%
250.00	2.521%	241.88	3.250%
300.00	0.697%	296.69	1.104%
350.00	0.788%	344.97	1.437%
400.00	0.465%	396.19	0.954%
450.00	0.308%	446.88	0.693%
500.00	0.303%	496.30	0.739%
550.00	0.118%	548.30	0.309%
600.00	0.201%	596.66	0.557%
650.00	0.028%	649.47	0.081%
700.00	0.134%	697.12	0.412%
750.00	0.024%	749.43	0.076%
800.00	0.088%	797.64	0.295%
850.00	0.044%	848.71	0.152%
900.00	0.056%	898.20	0.200%
950.00	0.047%	948.35	0.174%
1000.00	0.032%	998.79	0.121%
1050.00	0.043%	1048.23	0.168%
1100.00	0.014%	1099.39	0.056%
1150.00	0.037%	1148.28	0.150%
1200.00	0.000%	1200.00	0.000%

Figure 2: The relative error in the Kirchhoff transformation (2nd column); the obtained approximate temperature (3rd column); the relative error in the temperature (4th column), obtained with $N = 11$.

T	$\frac{\omega_{EX} - \omega_{APP}}{\omega_{EX}}$	T_{APP}	$\frac{ T - T_{APP} }{T}$
200.00	0.000%	200.00	0.000%
250.00	0.241%	249.21	0.318%
300.00	0.054%	299.74	0.087%
350.00	0.079%	349.49	0.145%
400.00	0.040%	399.67	0.083%
450.00	0.031%	449.68	0.071%
500.00	0.028%	499.66	0.067%
550.00	0.012%	549.82	0.032%
600.00	0.019%	599.68	0.053%
650.00	0.003%	649.95	0.008%
700.00	0.013%	699.72	0.040%
750.00	0.002%	749.95	0.007%
800.00	0.009%	799.77	0.029%
850.00	0.004%	849.88	0.014%
900.00	0.006%	899.82	0.020%
950.00	0.004%	949.85	0.016%
1000.00	0.003%	999.88	0.012%
1050.00	0.004%	1049.83	0.016%
1100.00	0.001%	1099.94	0.006%
1150.00	0.003%	1149.84	0.014%
1200.00	0.000%	1200.00	0.000%

Figure 3: The relative error in the Kirchhoff transformation (2nd column); the obtained approximate temperature (3rd column); the relative error in the temperature (4th column), obtained with $N = 31$.

Here we presented a mathematical support for representing the thermal conductivity as a piecewise constant function of the temperature, as well as exact formulae for the Kirchhoff transformation and its inverse, in a simple and complete way, without a limit of accuracy.

References

- [1] R.M.S. Gama, E.D. Corrêa, and M.L. Martins-Costa. An upper bound estimate for the steady-state temperature for a class of heat conduction problems wherein the thermal conductivity is temperature dependent. *International Journal of Engineering Science*, 69:77–83, 2013.
- [2] J.P. Holman. *Heat Transfer*. Raghathan Srinivasan, 2010.



ORIENTATION EFFECTS IN DISSIPATIVE STRUCTURES: NUMERICAL STUDY OF THE NONUNIFORMLY FORCED SWIFT-HOHENBERG EQUATION

Author: Daniel Coelho¹ danielcoelho.uerj@gmail.com
Advisors: José da Rocha Miranda Pontes¹ ; Norberto Mangiavacchi¹
¹ Rio de Janeiro State University

PPG-EM Seminars: season 2019
<http://www.ppgem.uerj.br>

February 14, 2020

Keywords: Pattern Formation, Computational Materials Science, Swift-Hohenberg Equation, Finite-Difference Methods

1 Introduction

Understanding selection and orientation mechanisms of spatial structures, their symmetries and instabilities represent a major theme of theoretical and experimental research in mathematical and computational modelling of self-organization phenomena. Spatio-temporal pattern formation is nowadays recognized to be related to several technological problems in physics, chemistry, nonlinear optics, and materials science [6]. The Swift-Hohenberg equation (SH)[4] is a widely accepted model not only for describing pattern formation in Rayleigh-Bénard systems but also for studying dynamics of phase transitions in liquid crystals and diblock copolymers [5, 3]. The numerical objective of this paper was to construct an efficient finite-difference time splitting scheme for solving the model. The second objective was to attain physically relevant results by examining structure behaviour in the presence of nonuniform forcings representations of the control parameter $\epsilon(\mathbf{x})$ [2, 1].

2 Mathematical modelling and numerical scheme

The SH equation has the so-called gradient dynamics, which means there is a potential, known as a Lyapunov functional, associated with the order parameter field $\psi(\mathbf{x}, t)$ that has the property of decreasing monotonically during the evolution. It can be derived by using the L^2 -gradient flow of the Lyapunov energy functional:

$$\mathcal{F}[\psi] = \int_{\Omega} d\mathbf{x} \frac{1}{2} \left\{ -\epsilon(\mathbf{x})\psi^2 + \alpha [(q_0^2 + \nabla^2)\psi]^2 + \frac{\beta}{2}\psi^4 + \frac{\gamma}{3}\psi^6 \right\}, \quad (1)$$

$$\frac{\partial \mathcal{F}[\psi]}{\partial t} = - \int_{\Omega} d\mathbf{x} \left(\frac{\partial \psi}{\partial t} \right)^2 \leq 0. \quad (2)$$

where Ω represents the domain whose size is commensu-

rate with the length scales of the patterns. We consider a regular domain $\Omega : \{x \in [0, L_x], y \in [0, L_y]\}$. $\epsilon(\mathbf{x})$ is the control parameter, $\alpha = 1$, $q_0 = 1$ ($\lambda_0 = 2\pi$), $\beta = -1$ and $\gamma = 0$ for the presented simulations. Also, Eq. (2) denotes the nonincreasing behaviour of the Lyapunov functional, which monotonically decreases until steady state is reached. By taking the variational derivative of Eq. 1 in L^2 norm, the following Swift-Hohenberg equation is obtained:

$$\frac{\partial \psi}{\partial t} = - \frac{\delta \mathcal{F}[\psi]}{\delta \psi}, \quad (3)$$

$$\frac{\partial \psi}{\partial t} = \epsilon(\mathbf{x})\psi - \alpha (q_0^2 + \nabla^2)^2 \psi + \beta \psi^3 - \gamma \psi^5. \quad (4)$$

In order to construct a Crank-Nicolson second order in time numerical scheme, we adopt the following representation proposed by Christov and Pontes (2002) [1] for the time derivative of Eq. 4, where the RHS is evaluated at the middle of the time step Δt :

$$\frac{\psi^{n+1,p+1} - \psi^n}{\Delta t} = \left(\Lambda_x^{n+1/2,p} + \Lambda_y^{n+1/2,p} \right) (\psi^{n+1,p+1} + \psi^n) + f^{n+1/2,p}, \quad (5)$$

where the index (p) refers to the internal iteration number. The superscript ($n+1, p+1$) identifies the new iteration, while (n) are the values of the previous time step. Internal iterations are required to secure a good approximation of the nonlinear term, i.e, until $\psi^{n,p}$ converges to $\psi^{n+1,p+1}$. The operators $\Lambda_x^{n+1/2,p}$, $\Lambda_y^{n+1/2,p}$ and $f^{n+1/2,p}$ are redefined as follows, for the SH equation:

$$\begin{aligned} \Lambda_x^{n+1/2,p} &= \frac{1}{2} \left[-\alpha \left(\frac{\partial^4}{\partial x^4} + \frac{q_0^4}{2} \right) - \beta \frac{(\psi^{n,p})^2 + (\psi^n)^2}{2} \right], \\ \Lambda_y^{n+1/2,p} &= \frac{1}{2} \left[-\alpha \left(\frac{\partial^4}{\partial y^4} + \frac{q_0^4}{2} \right) - \beta \frac{(\psi^{n,p})^2 + (\psi^n)^2}{2} \right], \\ f^{n+1/2,p} &= \frac{1}{2} \left[\epsilon(x, y) - \alpha \left(2q_0^2 \frac{\partial^2}{\partial x^2} + 2q_0^2 \frac{\partial^2}{\partial y^2} + 2 \frac{\partial^4}{\partial x^2 \partial y^2} \right) \right] (\psi^{n,p} + \psi^n), \end{aligned} \quad (6)$$

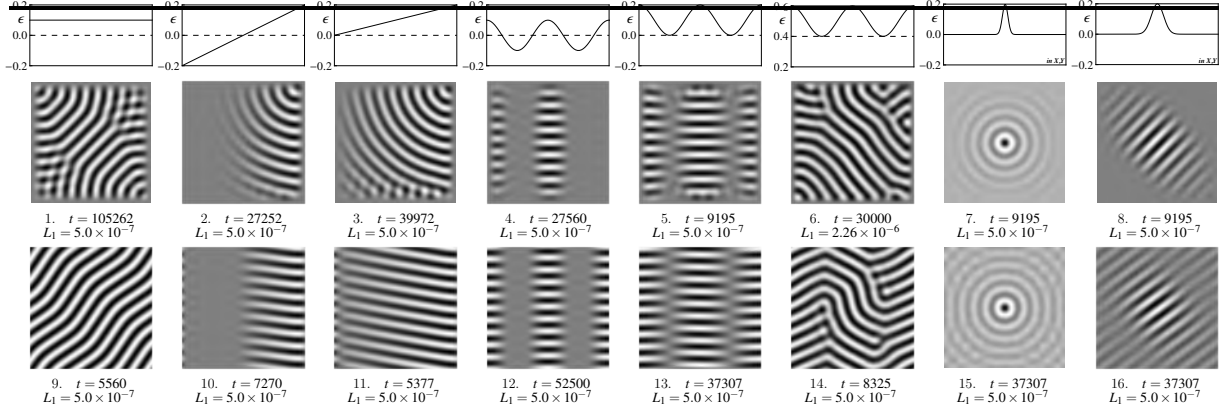


Figure 1: Structures numerically attained for nonuniform forcings distributions of the control parameter ϵ , represented in first row. Second and third rows have numerical results for RBC and PBC, respectively.

3 Numerical Experiments

All sixteen simulations in Fig. 1 have the same domain size ($10\lambda_0 \times 10\lambda_0$, i.e., 160×160 mesh points) and started from the same random initial conditions. We adopted rigid ($\psi = \partial\psi/\partial n=0$, where n stands for the outward normal direction to the boundary - RBC) and periodic boundary conditions (PBC), for comparison. Nonuniform forcings such as ramped, sinusoidal and gaussian distributions were adopted for $\epsilon(\mathbf{x})$. We assess the rate of change in time of the pattern during the simulation by monitoring the relative L_1 norm rate of change defined as:

$$L_1 = \frac{1}{\Delta t} \frac{\sum_{i,j} |\psi^{n+1} - \psi^n|}{\sum_{i,j} |\psi^{n+1}|}. \quad (7)$$

All simulations proceed until $L_1 \leq 5 \times 10^{-7}$, which is our criterion for reaching the steady state. Furthermore, by assessing a stricly evaluation of the Lyapunov functional we can observe free energy minimization in both RBC and PBC.

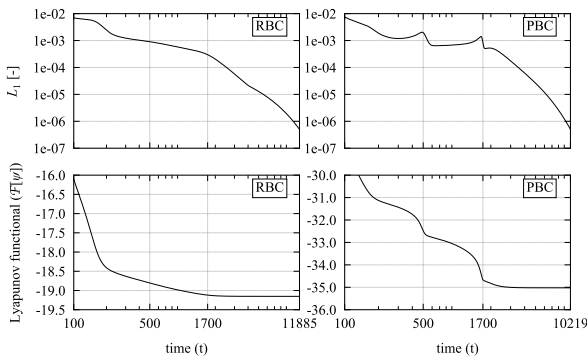


Figure 2: Test case: Strict evaluation of the Lyapunov functional evolution in time for RBC and PBC.

In Fig. 2 it is possible to notice that when defects are removed (L_1 peaks) there is a significant decrease of the Lyapunov functional. Also, PBC favors free-energy minimization until steady states are reached.

4 Conclusions

The main paper remarks are summarized as follows:

- The splitting scheme was proven to be uncondi-

tionally stable and consistent, serving as a reliable framework to numerically study the SH equation;

- Simulations show physical agreement with other numerical and observed experimental results;
- The nonuniform control parameter has a predominance in the pattern orientation for PBC instead of RBC (which implies the stripes to reach perpendicularly to the walls).
- Ramped and sinusoidal $\epsilon(\mathbf{x})$ in the subcritical region ($\epsilon < 0$) promotes a clear orientation in the gradient direction ($\nabla\epsilon(\mathbf{x})$).

5 Acknowledgments

The authors thank to CAPES for the Financial Support.

References

- [1] C.I. Christov and J. Pontes. Numerical scheme for swift-hohenberg equation with strict implementation of Lyapunov functional. *Mathematical and Computer Modelling*, 35, 2002. doi: 10.1016/S0895-7177(01)00151-0.
- [2] C.I. Christov, J. Pontes, D. Walgraef, and M.G. Velarde. Implicit time splitting for fourth-order parabolic equations. *Computer Methods in Applied Mechanics and Engineering*, 148, 1997. doi: 10.1016/S0045-7825(96)01176-0.
- [3] V. E. Podneks and I. W. Hamley. Landau-brazovski theory for the ia3d structure. *Journal of Experimental and Theoretical Physics Letters*, 64(8):617–624, 1996. doi: 10.1134/1.567271.
- [4] J. Swift and P. C. Hohenberg. Hydrodynamic fluctuations at the convective instability. *Physical Review A*, 15, 1977. doi: 10.1103/PhysRevA.15.319.
- [5] Eduardo Vitral, Perry H Leo, and Jorge Viñals. Role of gaussian curvature on local equilibrium and dynamics of smectic-isotropic interfaces. *Physical Review E*, 100(3):032805, 2019. doi: 10.1103/PhysRevE.100.032805.
- [6] D. Walgraef. *Spatio-Temporal Pattern Formation: With Examples from Physics, Chemistry, and Materials Science*. Partially Ordered Systems. Springer-Verlag New York, 1 edition, 1997. ISBN 978-1-4612-7311-0,978-1-4612-1850-0.



UASB (UPFLOW ANAEROBIC SLUDGE BLANKET) REACTORS SIMULATOR BASED ON ADM1

Author: Gabriel Oliveira¹ gabrielg_oliveira@hotmail.com
Advisor(s): Norberto Mangiavacchi¹

¹ Rio de Janeiro State University

PPG-EM Seminars: season 2019
<http://www.ppgem.uerj.br>

December 10, 2019

Keywords: ADM1, UASB, Finite Differences, Semi-Lagrangian.

1 Introduction

There is a big race around the world to reach alternative sources of energy and alternative ways of treating domestic sewage. UASB reactors (Upflow Anaerobic SludgeBlanket) have attracted attention due to their efficiency in the treatment of wastewater, in addition to presenting an efficient conversion of organic matter into gases such as methane, which can be used as an alternative source of energy. Due to these advantages that the UASB reactor has, there is a great force of implantation of this type ETS (effluent treatment station) in the domestic sewage network. In this work, the anaerobic digestion model ADM1 was studied and implemented in Octave software, to assemble a simulator that will assist in the design and operation of these types of anaerobic reactors, also enabling the future study of implementations of the ADM1 model.

2 Methodology

It was implemented in GNU Octave, an anaerobic digestion model known as ADM1, developed by the IWA (International Water Association) in 2002. The model consists of 24 stages, with 12 states related to soluble substrates, 5 states related to insoluble compounds and 7 states related to groups of bacteria [2]. The conservation equations coupled with the biological equations of soluble components described by ADM1 are presented in 2. For non-soluble ones, they are shown in 3. After the implementation of ADM1, a one-dimensional mesh with 25 nodes was built to simulate a 6-meter high reactor, the first node representing the entry condition. We use the first-order finite difference method in the Semi-Lagrangian algorithm to solve the differential equations. This method was developed by Sawyer at the beginning of the 1960s to integrate the conservation equation, the use of this method allows us to adopt much longer time steps [3]. The model features two speeds, hydraulic speed, and sedimentation speed. The sedimentation speed depends on several factors, such as the Reynolds number, the friction, the form factor, the convection currents induced in the fluid, the interactions between

the particles, the surface roughness of the particles, the effect of the wall [1]. This speed is updated at each iteration using Stokes' Law, according to the equation 1.

$$V_s = \frac{g(\rho_p - \rho_w)d^2}{18\mu} \quad (1)$$

$$\frac{dS_{liq,i}}{dt} = \frac{Q_{in}S_{in,i}}{V_{liq}} - \frac{S_{liq,i}Q_{out}}{V_{liq}} + \sum_{j=1-19} \rho_j v_{i,j} \quad (2)$$

$$\frac{dX_{liq,i}}{dt} = \frac{Q_{in}X_{in,i}}{V_{liq}} - \frac{X_{liq,i}Q_{out}}{t_{res,X} + \frac{V_{liq}}{Q}} + \sum_{j=1-19} \rho_j v_{i,j} \quad (3)$$

3 Results

The initial results were quite satisfactory, as they met the qualitative analysis of the observations made in the reactors in operation worldwide. In the first case, a simulation of a UASB reactor operating for 5 days with an HDT of 12h (Hydraulic Detention Time) and without any type of inhibition in biological processes was carried out. The affluent composition was only 0.5 kg * COD / m³ * d of complex compound. The first case is shown in Fig. 1, a pre-formation of sludge and a small production of methane was observed, this low production of methane gas is because the growth kinetics of methanogenic bacteria is very slow, therefore, practically not there was a production of methane gas. In the second case, at the beginning of the simulation, a certain concentration of consumers was placed inside the reactor, keeping all other parameters equal to the first case. We can observe an increase in methane production compared to the first case, as can be seen in Fig 2. The initial inoculation made the process more efficient in the production of methane gas, with this result we can show again that one of the essential factors is the size of the population of bacteria present in the sludge.

4 Conclusion

With the results obtained in these simulations of just 5 days, we can see that, by making some changes in

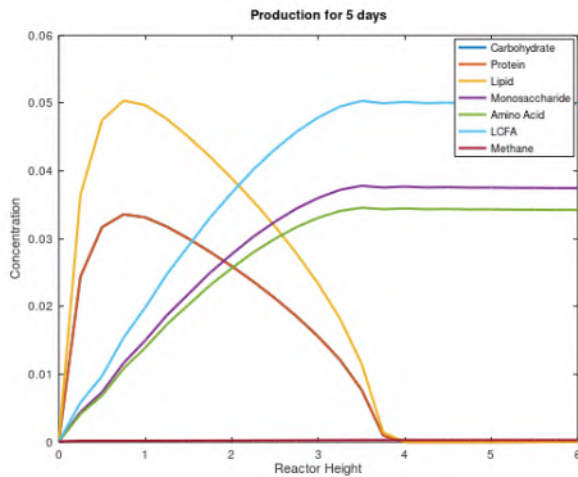


Figure 1: The concentration of particulates and solubles of interest inside a UASB reactor after 5 days of operation.

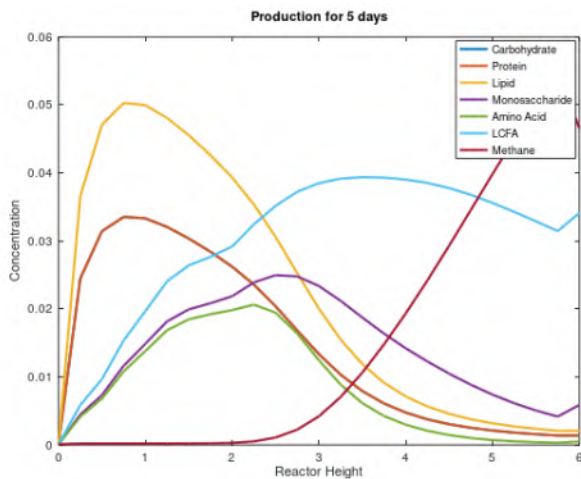


Figure 2: The concentration of particulates and solubles of interest inside a UASB reactor after 5 days of operation.

some parameters at the beginning of the simulation, we obtained different results in the production of methane. The simulation showed consistency with the real values, both in the processes of anaerobic digestion and in the hydraulic part, as well as in the process of sedimentation of the particles. As a result, this tool proved to be excellent for supporting projects, operations and research. The algorithm still needs some implementations, such as adding inhibitions inherent to the ADM1 model and placing the influence of temperature on anaerobic digestion processes

References

- [1] J. Alveirinho Dias. *A Análise Sedimentar e o Conhecimento dos Sedimentos Marinhos*. Universidade do Algarve Faro, 2004.
- [2] IWA Task Group for Mathematical Modelling of Anaerobic Digestion Processes. *Anaerobic digestion*

model no 1 (adm1). Technical report, IWA, First Edition London: IWA Publishing, 2002.

- [3] J. S. Sawyer. *A Semi-Lagrangian method of solving the vorticity advection equation*. ,vol. 15, pp. 336 342. Tellus, 1963.



MATHEMATICAL MODELLING AND SIMULATION OF TRANSIENT STATE HEAT TRANSFER PROCESS IN A RIGID BODY WITH TEMPERATURE-DEPENDENT THERMAL CONDUCTIVITY

Author: José Ricardo da Silva Cerqueira Junior¹
Advisor(s): Rogério Martins Saldanha da Gama¹

cerqueirajricardo@gmail.com

¹ Rio de Janeiro State University

PPG-EM Seminars: season 2019
<http://www.ppgem.uerj.br>

December 10, 2019

Keywords: temperature dependent thermal conductivity, Kirchhoff transformation.

1 Introduction

This paper is an initial proposal for my research during graduate studies. The aim is to solve the heat equation in a context which thermal conductivity is function of temperature. When solving a conduction heat transfer problem, it is common to use an approximation in which thermal conductivity is considered constant though that hypothesis is only valid under certain conditions. In order to get a better approximation for those cases and to make the numerical model easier to work with, we shall use a variable transformation known as Kirchhoff transformation.

2 Mathematical model

2.1 Heat equation

The temperature inside a rigid isotropic body, we shall call it Ω , can be calculated through the heat equation, [1]

$$\rho c \frac{\partial T}{\partial t} = \frac{\partial k \partial T}{\partial x^2} + \frac{\partial k \partial T}{\partial y^2} + \frac{\partial k \partial T}{\partial z^2} + \dot{q} \quad (1)$$

If we consider thermal conductivity k , as a constant, Equation (1) becomes:

$$\rho c \frac{\partial T}{\partial t} = \frac{k \partial^2 T}{\partial x^2} + \frac{k \partial^2 T}{\partial y^2} + \frac{k \partial^2 T}{\partial z^2} + \dot{q} \quad (2)$$

However Equation (3) should not be used if you are dealing with large differences of temperatures. In this case due the variation of thermal conductivity in function of temperature, the results numerically obtained can be far different from the reality.

In a preliminary study we shall adopt some hypothesis for the Equation (1):

- temperature known inside Ω in the initial instant
- temperature known over the surface of Ω at any moment

2.2 Kirchhoff transformation

In order to avoid dealing with an explicit relation between the temperature and thermal conductivity while solving the differential equation, we should use the Kirchhoff transformation. Let be w the Kirchoff transformation, [2]

$$w = \int_0^T k(\xi) d\xi \quad (3)$$

If we assume $k = \hat{k}$ as piecewise constant function of temperature [2], then we have:

$$\hat{k}(T) = \begin{cases} k_1, & T \leq T_1 \\ k_i, & T_i \geq T > T_{i-1}, \\ k_n, & T > T_{n-1} \end{cases}$$

That consideration gives better results the many parts, or values of k , the function have, and that lead us to linear equations for the Kirchhoff transformation and its reverse, [2]

$$w = \frac{1}{2}((k_1 + k_n)T + \sum_{i=2}^N (k_i - k_{i-1})(|T - T_{i-1}| - T_{i-1})) \quad (4a)$$

$$T = \frac{1}{2}((\frac{1}{k_1} + \frac{1}{k_n})w + \sum_{i=2}^N (\frac{1}{k_i} - \frac{1}{k_{i-1}})(|w - w_{i-1}| - w_{i-1})) \quad (4b)$$

3 Numerical model

In order to solve the Equation (1) we need to rewrite it in function of w :

$$\frac{1}{\alpha} \frac{\partial w}{\partial t} = \frac{\partial^2 w}{\partial x^2} + \frac{\partial^2 w}{\partial y^2} + \frac{\partial^2 w}{\partial z^2} + \dot{q} \quad (5)$$

Where α is the thermal diffusivity of the material and its value also depends on the temperature. We shall assume two hypothesis that are consequences of those from Equation (1) and of the rewritng of Equation (1) in function of Kirchhoff transformation. Those are:

- the value of Kirchhoff transformation is known over the surface of Ω at any moment
- the value of Kirchhoff transformation is known inside Ω in initial instant

We shall obtain the approximate solution of Equation (5) using:

$$\frac{1}{\alpha} \frac{w_{n-1}^{p+1} - w_{n-1}^p}{\Delta t} = \frac{w_{n-1}^{p+1} - 2w_n^{p+1} + w_{n-1}^{p+1}}{\Delta x^2} + \frac{w_{n-1}^{p+1} - 2w_n^{p+1} + w_{n-1}^{p+1}}{\Delta y^2} + \frac{w_{n-1}^{p+1} - 2w_n^{p+1} + w_{n-1}^{p+1}}{\Delta z^2} + \dot{q} \quad (6)$$

In that case as long as we know the values of w and the temperature at instant p , so we also have the value of thermal diffusivity in that moment. We shall use the value of α at instant p in Equation (6) to obtain the numerical solution getting a better approximation then using a constant value independent of temperature.

The values of w at the moment $p + 1$ obtained from Equation (6) can be used in Equation (4b) to calculate the reverse transformation and obtain the values of temperature inside the rigid body in that moment. The reverse transformation of Kirchhoff certainly exists if the values \hat{k} are above zero [2]. The value of w in a given temperature is:

$$w_i = \sum_{j=1}^i k_j (T_j - T_{j-1}) \quad (7)$$

4 Conclusions

This work is only beginning. Using the Kirchhoff transformation seems to be a good representation of reality since we have enough values of temperature, thermal conductivity and thermal diffusivity, besides, it is easier to deal with than using complicated numerical integrations and it is faster because demands less computational efforts.

The next steps we will take in this work are:

- to solve the problem with different boundary conditions like temperature unknown on the surface of the body, a convective heat flow over the surface and high temperatures in the neighborhood, when it is not possible to ignore the effects of radiation heat transfer.
- to compare the numerical solution with analytic results in order to validate the model.
- to apply that model in a project of some equipment like a reaction engine.

5 Acknowledgments

The author thanks to Prof. Rogério Gama for the advising, teaching and helping to develop his future dissertation.

References

- [1] Theodore L. Bergman; Adrienne S. Lavine; Frank P. Incropera; David P. Dewitt. *Fundamentos de Transferência de Calor e de Massa*. LTC, 2014.
- [2] R.M.S. Gama. Closed-form formulae for the kirchhoff transformation assuming a piecewise constant temperature dependent thermal conductivity. *Latin American Applied Research*, 47(2):53–57, 2017.



QUANTIFICATION OF DEFECTS IN THERMAL SPRAY COATINGS USING DIGITAL IMAGE PROCESSING

Author: Frederico G. B. Lacerda¹ fredericogarcia@live.com
Advisor(s): Marília G. Diniz¹

¹ Rio de Janeiro State University

PPG-EM Seminars: season 2019
<http://www.ppgem.uerj.br>

Dec 17, 2019

Keywords: Thermal spraying, coating, digital image processing.

1 Introduction

When mechanical components operate under harsh conditions and in harsh environments, coating their surfaces is an option for protection against corrosion and mechanical wear. Proper coating of a material can extend its life while maintaining its original mechanical properties while protecting against corrosion and wear.[2]

The thermal spray coating technique, especially that of electric arc coating, is characterized by flexibility in the choice of coating material, low thermal input to the substrate and virtually no dissolution thereof. In addition, the low operating cost, high deposition rate, good adhesion in the use of sealants and the possibility of field coating make the technique attractive.[1]

Metal coatings obtained by thermal spray are characterized by the deposition of successive layers of flattening and solidifying liquid droplets, resulting in a lamellar macrostructure. The metal droplets fuse and cool at an extremely high rate as they strike the substrate and mechanically anchor themselves to surface irregularities. A typical structure of spray coatings is comprised of sprayed material coverslips interspersed with oxide inclusions, cracks, unfused solid particles during the spraying process and porosity (Figura 1). The amount of these defects, essentially the trines and pores, will directly influence the coating properties.[3]

This work aimed to quantify the defects (cracks, pores and oxide nets) of two different coatings obtained by thermal spray technique through analysis and digital image processing obtained by optical microscopy.

2 Methodology

The coatings were applied on an 8 mm thick carbon steel plate (Table 1) properly prepared by Sa2 grade abrasive blasting with G16/20 mesh angular alumina.

The electric arc thermal spray was performed according to the parameters of Table 2 on a TAFE 8835 equipment:

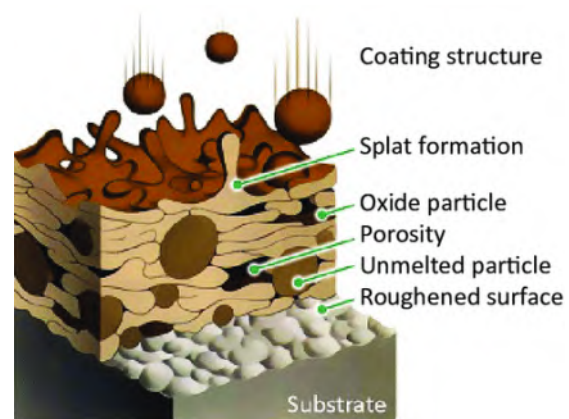


Figure 1: Typical structure of thermally sprayed coatings.

Table 1: Chemical composition of the substrate.

Element	% by weight
C	0,173
Mn	1,1
P	0,015
S	0,007
Cr	<0,05

Table 2: Thermal Spray parameters used.

Thermal Spray Parameters	
Voltage (V)	30
Current (A)	100
Atomizing Air Pressure (psi)	70
Projection Distance (mm)	100
Projection angle	90°
Deposition Rate (kg/h)	5

Two different metal alloys were used to make two different coatings, one called Alloy A and one Alloy B. (Table 3 and 4)

Table 3: Composition of consumable wires used to coat.

alloy A	% by weight
Cr	13,2
Nb	6,0
Ni	5,5
B	4,2
Al	2,0
Mn	1,3
Si	1,2
Fe	bal.

Table 4: Composition of consumable wires used to coat.

alloy B	% by weight
Cr	29,0
Mn	1,63
B	3,75
Si	1,6
Fe	bal.

Specimens were sectioned for the two coatings obtained from the coated plates. They were embedded and subjected to metallographic preparation until specular surfaces were obtained.

Thirty images were generated by optical microscopy without field overlap for each coating condition tested, all with 500x magnification.

The preprocessing, segmentation, postprocessing, and attribute extraction steps were performed using Fiji - Image J software to quantify the total defects present.

Figure 2 exemplifies the appearance of the coating before and after digital image processing. And figure 3 the software defect detection after processing, highlighting defects. From the demarcated area the percentage of defects for that image is calculated.

3 Results

Table 5 below contains the result for the analysis of the above-mentioned spray condition defects.

The results of digital image processing showed very

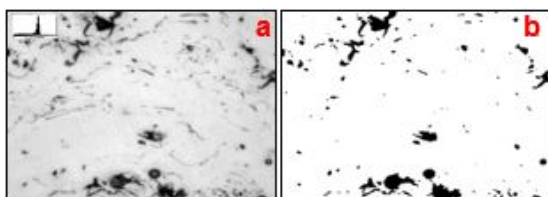


Figure 2: a) Image obtained by optical microscopy; b) Image after digital image processing.

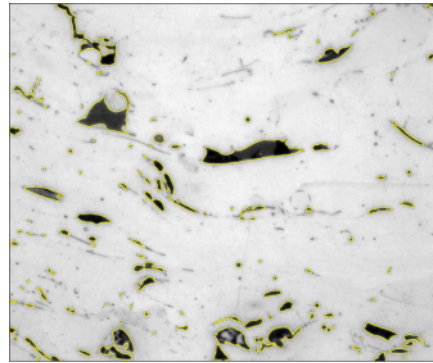


Figure 3: Defect identification, highlighting.

Table 5: Percentage of defects for each condition.

Specimen	Defects	Mean (%)
	Total	5,0
alloy A	Elongated	4,0
	Rounded	1,0
	Total	5,6
alloy B	Elongated	5,0
	Rounded	0,6

close values for the total number of defects in alloys A and B. The fraction of elongated defects was more present than the rounded defects in both alloys.

4 Conclusions

Based on the results, considering the different composition of the alloys, this fact reinforces the premise that the presence and morphology of defects depends mainly on the technique and the parameters applied in the thermal spraying.

5 Acknowledgments

The author thanks all the teachers, the advisor M.G. Diniz, PPG-EM/UERJ for their support, laboratory colleagues, and CAPES for funding the study.

References

- [1] D.L. GOMES. Caracterização de cinzas leves e de revestimento para caldeiras de central termelétrica brasileira. Master's thesis, FEN/UERJ, 2018.
- [2] S.S. KALSI, T.S. SIDHU, and H. SINGH. Characterization of nicraiy coatings on ni- and fe- based superalloys by the cold spray process. *Journal on Material Science*, 1, 2013.
- [3] Carlos Camello Lima and Roseana Trevisan. *Aspersão Térmica: Fundamentos e Aplicações*. Artliber, 2007.



OPTIMUM DESIGN OF AN URBAN BUS CHASSIS BASED ON GENETIC ALGORITHMS AND FINITE ELEMENT METHOD SIMULATIONS

Author: José Elias de Oliveira Gomes Júnior¹ josegomes.uerj@gmail.com
Advisors: Francisco José da Cunha Pires Soeiro¹ ; José Guilherme Santos da Silva²

¹ Universidade do Estado do Rio de Janeiro

² Universidade do Estado do Rio de Janeiro

PPG-EM Seminars: season 2019

<http://www.ppgem.uerj.br>

17 de Dezembro 2019

Keywords: Optimum Design, Structural Analysis, Genetic Algorithm, Finite Element Method

1 Introdução

Durante a vida útil de um chassi veicular, este é submetido a diferentes tipos de carga, dentre as quais são destaque e exercem papel fundamental no seu projeto as de flexão, torção e combinações destas, conforme [3]. Portanto, uma criteriosa análise estrutural sobre este elemento antes de projetá-lo tornou-se ponto chave antes de qualquer possibilidade de manufatura, como constataam [1].

Por definição, otimização é o ato de obter o melhor resultado dado dentre devidas circunstâncias. Em projetos de engenharia, seja em construção, manutenção ou em qualquer outra área, o objetivo será sempre obter o produto final através do menor esforço, ou com o maior benefício desejado possível. Uma vez que este menor esforço ou maior benefício geralmente podem ser expressos através de funções dependentes de determinadas variáveis, por exemplo, uma função $f(x)$, a otimização fica definido como a maximização ou a minimização da referida função $f(x)$. Também é importante ressaltar que se um determinado ponto é o valor máximo da função $f(x)$, o valor mínimo desta função pode ser obtido através da negativa, $-f(x)$, conforme [4].

2 Modelagem em Elementos Finitos

O chassi modelo B10M EDC 4x2 da Volvo do Brasil analisado consiste de uma estrutura metálica, fabricada com duas longarinas em perfil estrutural de aço em seção "C", de comprimento 9750 mm e por travessas soldadas transversalmente às longarinas. As travessas são perfis estruturais de seção retangular e totalizam 5 travessas com comprimento de 2460 mm e uma travessa de 824 mm, como é possível observar na figura 1. No que diz respeito às dimensões das seções retas dos perfis estruturais, pode-se verificar tais valores (em milímetros) na figura 2. O material especificado para a construção do chassi corresponde ao aço SAE 1020 cujas propriedades são apresentadas na tabela 1.

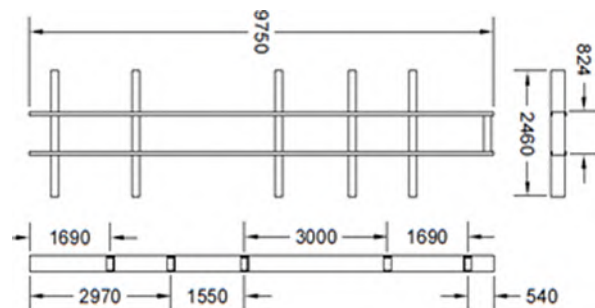


Figura 1: Sistema estrutural do chassi investigado

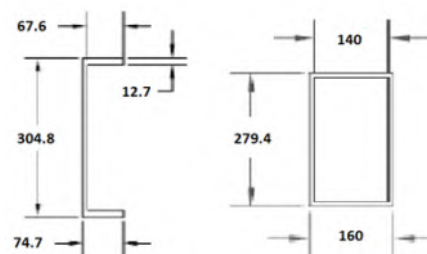


Figura 2: Seções retas dos perfis de aço

A modelagem por elementos finitos foi desenvolvida através do software ANSYS, utilizando o elemento SOLID45 de suas biblioteca e gerando uma malha de elementos sólidos tridimensionais hexaédricos de 8 nós, com 3 graus de liberdade por nó, cada um associado aos deslocamentos translacionais relativos aos três eixos cartesianos. O chassi em questão resultou em um modelo com 25128 nós e 12660 elementos finitos, em um total de 75384 graus de liberdade, tal como apresentado pela figura 3.

Para o modelo em elementos finitos foi realizada uma análise estática linear e, no que diz respeito às cargas, foram aplicados carregamentos uniformemente distribuídos na área superior das longarinas, ao longo de seu comprimento, onde todos os demais componentes do veículo são montados. Os carregamentos foram calculados em função da capacidade técnica de carga de 17700 kgf, especificada pela Volvo do Brasil. A distribuição

Propriedade	Valor
Módulo de Elasticidade Longitudinal	205 GPa
Massa Específica	7870 kg/m ³
Coefficiente de Poisson	0,29
Tensão Limite de Escoamento	350 MPa

Tabela 1: Propriedades mecânicas do aço SAE 1020

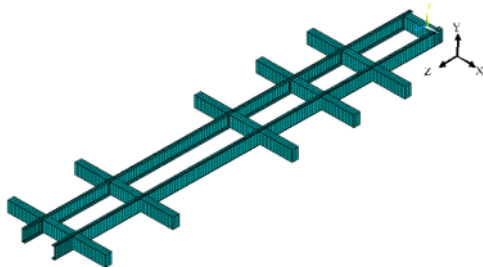


Figura 3: Modelo numérico em elementos finitos do chassi utilizando-se o elemento finito SOLID45

das tensões equivalentes de Von Mises está disposta na figura 4 e atinge o valor máximo de 68,1 MPa.

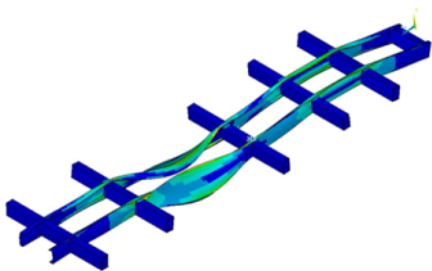


Figura 4: Distribuição de tensões de Von Mises atuantes sobre o chassi (Unidade: Pa)

3 Otimização pelo Algoritmo Genético

A otimização da estrutura deve seguir a equação 1.

$$\sigma_p = \frac{\sigma_e}{FS} \quad (1)$$

Onde σ_e é a Tensão Limite de Escoamento do material, aço SAE 1020, que equivale a 350 MPa e FS é o fator de segurança do projeto, que para fins de análise estática em chassis do tipo escada, é comumente utilizado como 3.0 conforme [2].

A função objetivo que deve ser minimizada é a massa do veículo, representada pela equação 2. Nela, as variáveis $W1$, $W2$, $W3$, $T1$, $T2$, $H2$ e $H3$ são as dimensões dos perfis estruturais e estas serão alteradas conforme a disponibilidade comercial dos perfis. $C1$, $C2$ e $C3$ são comprimentos fixos das longarinas e das travessas e são mantidas constantes.

$$m = d[(2W1T1 + T2H2)(2C1) + (W2H2 - W3H3)(6C2 + 10C3)] \quad (2)$$

Para otimizar a estrutura é necessário determinar os

parâmetros inerentes ao AG no MATLAB, como taxa de crossover (70%), taxa de mutação (10%), número de gerações (100) e população inicial (150). O funcionamento correto da otimização aqui proposta depende da correta implementação entre a interface mista entre o MATLAB e o ANSYS.

4 Resultados e Discussão

A utilização de 100 gerações com populações de 150 indivíduos em cada totalizou 15000 iterações, ou seja, foram criados 15000 indivíduos que foram testados na função objetivo e levados ao ANSYS para as análises estruturais. Após as 15000 iterações realizadas pelo Algoritmo Genético, o mínimo global da função objetivo foi alcançado, apresentando assim a solução ótima do problema. A Figura 7 apresenta a evolução dos valores da função penalidade em cada geração do AG, além disso, são apresentados o melhor resultado e a média dos resultados por geração para esta função. O melhor valor encontrado é a massa mínima do chassi, $m = 523.32$ kg.

Deve-se mencionar que o ponto crítico, i.e., o de maior tensão na estrutura é o mesmo na estrutura otimizada e antes da otimização, o que corrobora a integridade do processo de otimização, já que o mesmo não altera as características de projeto da estrutura. O que ocorre é a diminuição das seções dos perfis transversais e, logo, da massa e o aumento da tensão no ponto crítico, já que a carga que o chassi deve suportar não é alterada.

5 Conclusão

O presente trabalho concluiu que é possível desenvolver uma metodologia de otimização para chassis de ônibus urbanos a partir de uma interface apropriada entre o AG e o ANSYS, de forma que no estudo de caso real apresentado foi possível obter uma redução de massa em comparação com a configuração original de projeto. A otimização, embora a partir de hipóteses simplificadoras, resultou em uma redução mássica da ordem de 64%. Logo, para que este chassi seja efetivamente fabricado é necessário que seja realizada uma análise dinâmica do componente, ao invés de utilizar somente o fator de segurança recomendado pela literatura.

Referências

- [1] R. Cazacu et. al. Structural optimization with genetic algorithms and particle swarm optimization. *Proceedings of the Annual Session of Scientific Papers*, 12:19–22, 2013.
- [2] V. Francis et. al. Structural analysis of ladder chassis frame for jeep using ansys. *International Journal Of Modern Engineering Research (IJMER)*, 4, 2014.
- [3] V. Rahul et. al. Structural analysis of pick-up truck chassis using fem. *International Journal of Chem-Tech Research*, 9:384–391, 2016.
- [4] S. Rao. *Engineering Optimization: Theory and Practice*. JohnWiley Sons, 2009.



USE OF FOCUSED ION BEAM OF GALLIUM AND HELIUM FOR LITHOGRAPHIC DRAWINGS OF METROLOGICAL PATTERNS IN A SILICON SAMPLE

Author: Matheus Costa Ximenes¹ matheus.costa.ximenes@gmail.com
Advisor(s): José Brant de Campos¹

¹ Rio de Janeiro State University

PPG-EM Seminars: season 2019
<http://www.ppgem.uerj.br>

Dec 17, 2019

Keywords: Nanometrology. Nanopatterning. Helium Beam Microscopy. Sputtering.

1 Introduction

An important instrument that successfully meets nanotechnological and nanometrological challenges is the focused ion beam microscope (FIB). This technology offers unparalleled opportunities for direct removal or deposition of material on a solid surface, and this can be accomplished at nanoscale dimensions. [4]

Most modern FIB systems use a liquid metal source, field gas source, or plasma source to produce variable current ion beams, mostly double or triple beam. The present work used a triple beam focused ion beam microscope, such a microscope contains two ion emission columns: one more traditional with liquid metal ion source, emits Gallium ions and another with gas ion source, can be used individually in this column both Neon gas and Helium gas. A triple beam FIB has the same characteristics as a traditional double beam, however the function of the electron beam is the gas source ion beam, which can be responsible for images with very high quality and resolution, and may be higher when compared to images from a dedicated SEM. [1]

In this study we investigated the influence of gallium and helium ion beam defects on silicon by comparing metrologically whether an ion beam microscope actually provides the programmed patterns.

2 Methodology

2.1 Instruments and sample

The generation of the lithographic drawings of the patterns was performed using a Zeiss HIM Orion NanoFab triple-beam microscope from DIMAT (Materials Metrology Division) at the National Institute of Metrology, Quality and Technology (INMETRO).

For the observation of defects produced by nanolithography, was used or field emission gun scanning electron microscope (SEM-FEG), the Jeol JSM-7100F Thermal field emission electron microscope from the Nanofabrication and Characterization of Nanomaterials

(NANOFAB), State University of Rio de Janeiro.

The samples on which the lithographic nanopatterns were designed were of Czochralski oriented (100) monocrystalline silicon.

2.2 Silicon Experiment

Using the triple beam FIB, they were drawn on a sample of oriented silicon of approximate dimensions of 10mm x 8mm, a calibration cross and two nanopatterns:

a) Pattern drawn using the gallium ion beam (Ga⁺), located approximately in the center of the sample. The pattern was drawn over an area of 0.5mm x 0.5mm, and 121 squares were drawn with 1.5 μ m sideways, 50mm apart isometrically, from their upper left edge. Four 50 μ m x 50 μ m crosses were drawn around the pattern for easy identification. A dosage of $6 \times 10^{17} \text{ cm}^{-2}$ was used for gallium beam scans.

b) Pattern drawn using the helium ion beam: Located in one of the spaces of the previous pattern, more precisely, in the last row of the first column, the pattern was drawn over an area of 5.5 μ m x 5.5 μ m, and 289 squares 9nm sideways, isometric distances approximately 340nm from each other from their upper left end. A $6 \times 10^{17} \text{ cm}^{-2}$ dosage was used for Helium beam scans.

MEV-FEG images of the gallium beam pattern were acquired using a 5 keV acceleration energy and 4.0 mm working distance and MEV-FEG images of the helium beam pattern were acquired using a 0.5 keV acceleration energy and 1.7 mm working distance.

3 Results and Discussion

Figures 1 and 2 show images acquired by the SEM-FEG, where it is possible to observe the linear distance between two markings made by the FIB with the gallium and helium beam, respectively, either on the x axis or on the y axis.

Because gas sources generate ions of smaller atomic mass and size when compared to liquid metal sources, their sample damage is reduced and consequently the sample sputtering rate is also reduced, which impairs

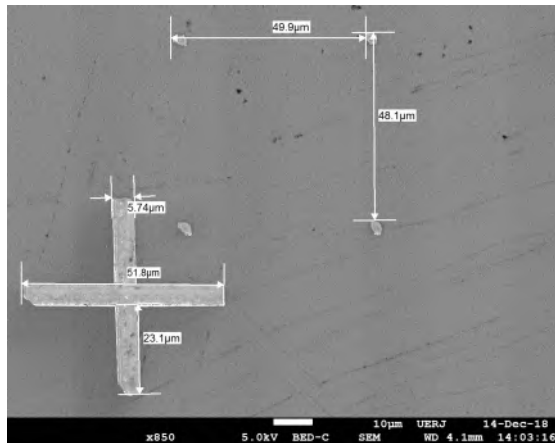


Figure 1: SEM-FEG images containing linear distance measurements between two markings of the pattern drawn by the gallium beam

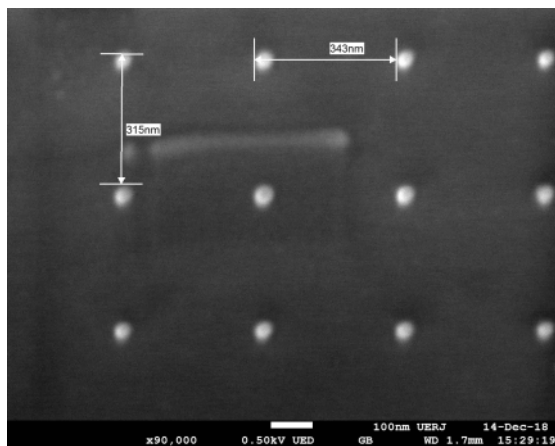


Figure 2: SEM-FEG images of linear distance measurements between two helium pattern markings

the milling speed of a sample, but increases accuracy. The helium sputtering rate is two orders of magnitude smaller than gallium at comparable beam energies, so the helium beam strikes the sample much more smoothly and can make marks on much smaller scales [3]

A sampling of 40 measurements between the gallium and helium excavations was collected, 20 vertical and 20 horizontal in each pattern. Thus obtaining the average distance and standard deviation, respectively $48.90\mu\text{m}$ and $1.28\mu\text{m}$ for the Gallium beam and 334nm and 13nm for the Helium beam. Dividing the average distance by the programmed value gives a decrease in excavation distance of 2.2 percent for Gallium and 1.7 percent for Helium.

It can be seen that the FIB mask programming for the gallium and helium beams, when applied to the sample and analyzed, had similar dimensions to the measurements made by the SEM-FEG.

Observation of the patterned region using an MEV-FEG device is compromised when smaller doses are used or when the distance between points is reduced, such as the helium beam pattern. In future work, it may be

easier to observe the patterns under these conditions using an atomic force microscopy (AFM) apparatus. [2]

4 Conclusions

Using the FIB technique, we generated defects in a silicon sample in the form of a pattern where metrological analysis was possible using the SEM microscope. This can be used as a metrological tool to compare different FIB and MEV machines, and may contribute to the development of the equipment, as well as being a starting point for the creation of metrological calibration standards for both nanometer-scale devices. [2]

In short, it has been shown in this study that direct writing in silicon patterns via the gallium and helium ion beam can provide new metrological results, and this fact can greatly contribute to the development of nanotechnology for materials. With future work in mind, new patterns can be made from the Gallium and Helium beams, varying the dosage, operating voltage, number of beams in a given region, and the shape of the pattern. The addition of Neon beam excavated patterns can be performed, as the FIB used has this possibility, considerably increasing its scope. Finally, for a better analysis of the patterns the atomic force microscopy technique can be used.

5 Acknowledgments

We thank Inmetro for making the triple beam FIB available for this work and Nanofab, especially Dr. Vitor and Dr. Hirschel for making MEV-FEG available and operating for this work.

This work was carried out with the support of the Higher Education Personnel Improvement Coordination - Brazil (CAPES) - Financing Code 001.

References

- [1] S. Bauerdik. Nanofabrication using focused ion beams. *Microscopy and Analysis*, 153:11–13, 2018.
- [2] B. S. Archanjo et al. Ion beam nanopatterning and micro-raman spectroscopy analysis on hopg for testing fib performances. *Ultramicroscopy*, 111: 1338–1342, 2011.
- [3] M. S. Joens et al. Helium ion microscopy (him) for the imaging of biological samples at sub-nanometer resolution. *Scientific Reports*, 3:3514, 2013.
- [4] N. Yao. *Focused Ion Beam Systems: Basics and Applications*. Cambridge University Press, 2007.

